Finite Element Simulation of Intimal Thickening in 2D Multi-Layered Arterial Cross Sections by Morphoelasticity

Pak-Wing Fok,
Dept. of Mathematical Sciences,
University of Delaware,
DE 19716, USA
pakwing@udel.edu

Kun Gou,
Dept. of Science and Mathematics,
Texas A&M University – San Antonio,
TX 78224, USA
kgou@tamusa.edu

January 27, 2020

Abstract

Morphoelasticity is a framework commonly employed to describe tissue growth. Its central premise is the decomposition of the deformation gradient into the product of a growth tensor and an elastic tensor. In this paper we present a 2D finite element method to solve compressible morphoelasticity problems in arterial cross sections. The arterial wall is composed of three layers: the intima, media and adventitia. The intima is allowed to grow isotropically while the areas of the media and adventitia are approximately conserved. All three layers are modeled as Holzapfel-Gasser-Ogden type anisotropic hyperelastic materials with different mechanical parameters.

This paper consists of three main contributions. First, a new energy functional that underpins the finite element method for morphoelasticity is presented. The bulk energy is associated with elastically deforming *grown* elements, rather than elements in the reference configuration which is the usual practice in classical hyperelasticity. A surface energy describes live pressure loading through a lumen blood pressure. We derive the equivalent weak form and show that stationary points correspond to the usual boundary value problem for mechanical equilibrium.

Second, we present the details of a displacement-based morphoelastic finite element method. The primary variable for our method is the deformation, which we separate

into two groups (horizontal and vertical deformations). We arrive at a system of non-linear algebraic equations that are organized into self-contained blocks which can be assembled independently. We present a method to compute the Jacobian of this system which is fed into a Newton algorithm. The direction of collagen fibers in each layer is computed off-line by interpolating tangent vectors from nearby boundaries and a minimum norm solution for the grown and deformed artery is found by the QR factorization. This single-field approach produces reasonable numerical results, although the locking phenomenon is clearly present. For axisymmetric meshes, our position and stress fields are validated by the solution obtained from solving a system of ordinary differential equations.

Finally, we use the code to simulate intimal thickening in pseudo-realistic arterial cross sections. We find that (i) Oscillations in the lumen-intima interface are unstable and amplify with growth (ii) Glagov remodeling occurs with lumen area initially increasing and then decreasing with growth and (iii) Maximum stresses migrate from the lumen-intima interface to the media-intima interface so that the media eventually bears the maximum stress.

Keywords: Intimal Thickening, Atherosclerosis, Morphoelasticity, Hyperelasticity, Tissue growth, Finite element method.

1   Introduction

In this paper we present a finite element method for simulating intimal thickening in arteries using morphoelasticity theory. Morphoelasticity theory is essentially a theory of growth applied to hyperelastic solids [1, 2]. The underlying assumption is that the deformation gradient $\mathbf{F}$ is decomposed into a product of an elastic tensor $\mathbf{F}_e$ and a growth tensor $\mathbf{G}$

$$\mathbf{F} = \mathbf{F}_e \mathbf{G}, \tag{1}$$

and strain energy densities are functions of the *elastic* deformation gradient $\mathbf{F}_e$. Our method simulates the growth and deformation of 2D arterial cross sections using finite elements. The method is presented purely in terms of node positions and uses triangular elements and piecewise linear basis functions. Finding the stationary points of the resulting energy functional is performed using Newton's method.

The biomechanical simulation of arteries presents some issues that are unique to arterial tissue modeling. Some of these are:

1. Arteries consist of three layers, each with specific mechanical properties. The intima is the innermost layer, followed by the media which is surrounded by the adventitia. In this paper we model all three layers by HGO (Holzapfel-Gasser-Ogden) type strain energy functions [3, 4, 5]. The layers are separated by thin elastic laminas.

2. As the name suggests, in intimal thickening, growth mainly occurs in the intima. In balloon-injury experiments on animals [6, 7], this growth results from the migration of smooth muscle cells from the media, in response to the release of Platelet-Derived Growth Factor (PDGF).

2

3. The body is anisotropic due to the presence of embedded collagen fibers. These fibers are ordered in a helical fashion, rendering the artery wall harder to dilate than to stretch in the axial direction, for example. The strain energy density at any point in the vessel wall depends on the local orientation of these fibers. Our method computes these orientations by interpolating tangent vectors from the two closest laminas.

Intimal thickening is a common condition that occurs naturally as one ages. There are two types of intimal thickening: eccentric and diffuse [8]. Eccentric intimal thickening (also known as "intimal cushions") are localized accumulations of intima tissue, usually occuring at bifurcations in the artery. On the other hand, diffuse intimal thickening (DIT) can also occur along non-branching sections of the artery and spreads circumferentially and axially. Its structure consists of smooth muscle cells, elastin and proteoglycans. Importantly, no lipids and very few macrophages are present and neo-vascularization, vasa vasora and calcification are all absent. All these factors distinguish DIT from atherosclerosis. However, DIT is considered a precursor to atherosclerosis in that the neo-intima from DIT forms the "soil" in which atherosclerosis is supposed to develop [9]. The method presented in this paper is 2D and does not describe the axial spread of disease; however the results we present qualitatively resemble DIT in which lesions are fairly concentric.

Our method is presented in terms of the horizontal and vertical position fields x and y. Upon discretizing the total energy functional, we set the x and y gradients to zero to set up a root-finding problem. By separating the primary variables into two groups, we arrive at a system of nonlinear algebraic equations that are organized into self-contained blocks that can be computed and assembled independently. From our functional, we derive an expression for the Jacobian that is assembled element-by-element and underpins the Newton-Raphson iteration. The block structure of the equations and availability of the Jacobian allows a streamlined implementation of the method. Because our method solves for the position fields only, it is very susceptible to locking, especially for values of the Poisson ratio close to 1/2. For small/moderate values of ν (e.g. $\nu \sim 0.1 - 0.3$), the position fields are generally smooth and accurate. For $\nu \gtrsim 0.45$, locking is more prominent and stress fields often present a "checkerboard" instability.

Morphoelasticity is not the only paradigm for tissue growth. For example, there is a related swelling theory that has been applied to tracheal tissue [10] and one can also describe the growth of tissues using mixture theory [11, 12]. Nevertheless, computational morphoelasticity within a finite element framework is popular within the engineering community and has been used to model cerebral aneurysms [11] and skin [13] as well as idealized arteries [14]. From our literature search, most computational studies on arteries assume that the vessel wall is homogeneous [14, 15, 16], ignoring the fact that it is composed of three distinct layers with different growth rates and mechanical properties. In this contribution, we model the wall as three mechanically different structures that are bonded together and pay special attention to the intima which is assumed to be the only growing layer. Although we effectively treat growth as an independent parameter, it can also be modeled as a diffusing molecular messenger [17] or be stress-induced [15].

This paper is organized as follows. In section 2, we present the energy functional which forms the foundation of our finite element method. From this functional, we derive the

corresponding weak form and show that it is equivalent to the usual boundary value problem associated with mechanical equilibrium. In section 3, we explain the energy functional in more detail and discuss how collagen fiber directions can be computed and the way their energies can be incorporated into the functional. In section 4 we show how to implement the numerical method by assembling the governing algebraic system in blocks and solving it using the Newton-Raphson method. In section 5 we present simulation results of an artery undergoing intima thickening and monitor the stress in individual layers. Finally in section 6 we summarize our results and discuss weaknesses and strengths of our model. The appendix explains how to assemble the Jacobian matrix associated with the Newton Raphson method and also gives details on setting up and solving a multi-layered axisymmetric model.

2   Energy Functional for Morphoelastic Bodies
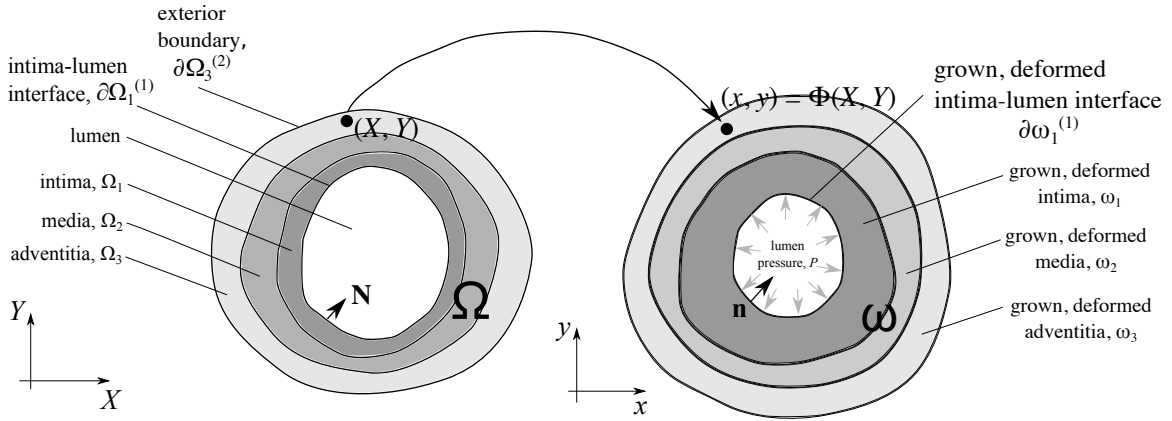
Figure 1: Cross section of an artery showing the lumen, intima, media and adventitia. The reference configuration $\Omega = \bigcup_{k=1}^{3} \Omega_k$, is mapped to the grown and deformed configuration $\omega = \bigcup_{k=1}^{3} \omega_k$ and the reference point (X, Y) is mapped to the point (x, y). The unit normal vector $\mathbf{N}$ points into the reference-configuration lumen while $\mathbf{n}$ points into the grown and deformed lumen. The inner and outer boundaries of Ω_k are $\partial\Omega_k^{(1)}$ and $\partial\Omega_k^{(2)}$ respectively for $k = 1, 2, 3$ in the reference frame. These boundaries map to $\partial\omega_k^{(1)}$ and $\partial\omega_k^{(2)}$ in the grown, deformed frame.

Consider a multi-layered, hyperelastic, annular cylinder that is infinite in the axial direction, Z. The material properties of the cylinder are assumed to be invariant with respect to Z and we assume that deformations are also invariant with respect to Z. Due to these symmetries, the growth and deformation of the cylinder are completely defined by considering a single Z-slice represented in Fig. 1. We divide the domain Ω into three subdomains, corresponding to each of the layers: $\Omega = \Omega_1 \cup \Omega_2 \cup \Omega_3$ where Ω_1, Ω_2 and Ω_3 represent the intima, media and adventitia respectively. Notationally, we define $\partial\Omega_k^{(1)}$ and $\partial\Omega_k^{(2)}$ to be the the inner and outer boundaries of Ω_k respectively. Hydrostatic pressures P_1 and P_2 are

applied on $\partial\Omega_1^{(1)}$ and $\partial\Omega_3^{(2)}$; a no traction boundary condition on the outer boundary (for example) corresponds to $P_2 = 0$.

The deformation is assumed to be continuous across $\partial\Omega_1^{(2)}$ and $\partial\Omega_2^{(2)}$; and $\partial\Omega_1^{(2)}$ ($\partial\Omega_2^{(2)}$) is geometrically the same contour as $\partial\Omega_2^{(1)}$ ($\partial\Omega_3^{(1)}$). In classical hyperelasticity, for a given deformation $\mathbf{\Phi}$, $\mathbf{F} = \nabla\mathbf{\Phi}$ is the deformation gradient and the stored elastic energy per unit length in the axial direction would be

$$\Pi_{\text{hyp}}[\mathbf{\Phi}] = \int_\Omega W(X,Y,\mathbf{F})dA + \frac{P_1}{2}\int_{\partial\Omega_1^{(1)}} J\mathbf{F}^{-T}\mathbf{N}\cdot\mathbf{\Phi}dS + \frac{P_2}{2}\int_{\partial\Omega_3^{(2)}} J\mathbf{F}^{-T}\mathbf{N}\cdot\mathbf{\Phi}dS. \quad (2)$$

where

$$\mathbf{\Phi} = (\Phi_1(X,Y),\Phi_2(X,Y),Z)^T,$$

$$\mathbf{F} = \nabla\mathbf{\Phi} = \begin{bmatrix} \frac{\partial\Phi_1}{\partial X} & \frac{\partial\Phi_1}{\partial Y} & 0 \\ \frac{\partial\Phi_2}{\partial X} & \frac{\partial\Phi_2}{\partial Y} & 0 \\ 0 & 0 & 1 \end{bmatrix}, \quad (3)$$

$$J = \det\mathbf{F},$$

$$\mathbf{N} = (N_1,N_2,0)^T. \quad (4)$$

Because we consider arterial domains that have different material properties in different subdomains of Ω, W may take different functional forms depending on whether (X,Y) is in the intima, media, or adventitia:

$$W(X,Y,\mathbf{F}) = \begin{cases} W_1(\mathbf{F}), & (X,Y) \in \Omega_1, \\ W_2(\mathbf{F}), & (X,Y) \in \Omega_2, \\ W_3(\mathbf{F}), & (X,Y) \in \Omega_3. \end{cases} \quad (5)$$

The surface energies in eq. (2) have $1/2$ prefactors in front of the integrals. For problems involving a general deformation in the X,Y and Z directions, the prefactors multiplying the surface integrals are $1/3$ [18, 19, 20].

We now assume that the cylinder is *morphoelastic* instead of hyperelastic, with each layer characterized by a constant growth tensor:

$$\mathbf{G}(X,Y) = \begin{cases} \mathbf{G}_1, & (X,Y) \in \Omega_1, \\ \mathbf{G}_2, & (X,Y) \in \Omega_2, \\ \mathbf{G}_3, & (X,Y) \in \Omega_3, \end{cases}$$

and $\mathbf{G}_k$, $k = 1,2,3$ are constant tensors. Likewise, define

$$J_g = \begin{cases} \det\mathbf{G}_1, & (X,Y) \in \Omega_1, \\ \det\mathbf{G}_2, & (X,Y) \in \Omega_2, \\ \det\mathbf{G}_3 & (X,Y) \in \Omega_3. \end{cases}$$

For a three-layered morphoelastic annular cylinder, eq. (2) generalizes to

$$\Pi[\mathbf{\Phi}] = \sum_{k=1}^3 \int_{\Omega_k} J_{g,k}\cdot W_k(\mathbf{F}_e)dA + \frac{P_1}{2}\int_{\partial\Omega_1^{(1)}} J\mathbf{F}^{-T}\mathbf{N}\cdot\mathbf{\Phi}ds + \frac{P_2}{2}\int_{\partial\Omega_3^{(2)}} J\mathbf{F}^{-T}\mathbf{N}\cdot\mathbf{\Phi}dS \quad (6)$$

where

$$\mathbf{F}_e = \mathbf{F}\mathbf{G}^{-1} = (\nabla\mathbf{\Phi})\mathbf{G}^{-1}, \tag{7}$$

$$J = \det\mathbf{F}, \tag{8}$$

$$J_{g,k} = \det\mathbf{G}_k. \tag{9}$$

The growth Jacobian, J_g is a piecewise constant function on Ω and $J_{g,k}\cdot W_k dA$ in (6) represents the potential energy of a *grown* infinitessimal element dA. When $J_g = 1$, the morphoelasticity functional reduces to the hyperelasticity functional (2) and the energy depends on how material elements dA are elastically strained. However, when $J_g > 1$, elements undergo stress-free growth before they are strained: the correct energy to use depends on elastic deformations of grown elements with area $J_g dA$.

Now we prove that stationary point of (6) solves the BVP corresponding to mechanical equilibrium. Let

$$E_1 = \sum_{k=1}^{3} \int_\Omega J_{g,k} \cdot W_k(\mathbf{F}_e) dA, \tag{10}$$

$$E_2 = \frac{P_1}{2} \int_{\partial\Omega_1^{(1)}} J\mathbf{F}^{-T}\mathbf{N} \cdot \mathbf{\Phi} dS, \tag{11}$$

$$E_3 = \frac{P_2}{2} \int_{\partial\Omega_3^{(2)}} J\mathbf{F}^{-T}\mathbf{N} \cdot \mathbf{\Phi} dS. \tag{12}$$

Suppose $\Pi[\mathbf{\Phi}]$ is stationary. Then the Gateaux derivative of Π at $\mathbf{\Phi}$ must be zero:

$$\Pi'[\mathbf{\Phi}]\mathbf{\Phi}' \equiv \left.\frac{d}{d\varepsilon}\Pi[\mathbf{\Phi} + \varepsilon\mathbf{\Phi}']\right|_{\varepsilon=0} = 0, \tag{13}$$

for all $\mathbf{\Phi}' = (\Phi_1', \Phi_2', 0)^T$ and we introduced a small perturbation to $\mathbf{\Phi}$ that gives rise to perturbations in $\mathbf{F}$ and $\mathbf{F}_e$:

$$\mathbf{F} \to \mathbf{F} + \varepsilon\mathbf{F}' \implies \mathbf{F}_e \to \mathbf{F}_e + \varepsilon\mathbf{F}_e', \tag{14}$$

where $\mathbf{F}_e' = \mathbf{F}'\mathbf{G}^{-1} = (\nabla\mathbf{\Phi}')\mathbf{G}^{-1}$ and $\mathbf{F}_e = \mathbf{F}\mathbf{G}^{-1} = (\nabla\mathbf{\Phi})\mathbf{G}^{-1}$. We now find the Gateaux derivatives of E_1, E_2 and E_3 in the direction of $\mathbf{\Phi}'$.

- Gateaux derivative of E_1.

$$
\begin{aligned}
E_1'[\mathbf{\Phi}]\mathbf{\Phi}' &= \frac{d}{d\varepsilon} \sum_{k=1}^{3} \int_{\Omega_k} J_{g,k} \cdot W_k(\mathbf{F}_e + \varepsilon \mathbf{F}_e') dA \bigg|_{\varepsilon=0} \\
&= \sum_{k=1}^{3} \int_{\Omega_k} J_{g,k} \cdot \frac{\partial W_k}{\partial \mathbf{F}_e} : \mathbf{F}_e' dA \\
&= \sum_{k=1}^{3} \int_{\Omega_k} J_{g,k} \cdot \frac{\partial W_k}{\partial \mathbf{F}_e} : \mathbf{F}' \mathbf{G}_k^{-1} dA \\
&= \sum_{k=1}^{3} \int_{\Omega_k} \left(J_{g,k} \frac{\partial W_k}{\partial \mathbf{F}_e} \mathbf{G}_k^{-T} \right) \mathbf{G}_k^{T} : (\nabla \mathbf{\Phi}') \mathbf{G}_k^{-1} dA \\
&= \sum_{k=1}^{3} \int_{\Omega_k} \mathbf{T}_k \mathbf{G}_k^{T} : (\nabla \mathbf{\Phi}') \mathbf{G}_k^{-1} dA.
\end{aligned}
$$

Note that in compressible morphoelasticity, the first Piola Kirchoff stress is $\mathbf{T} = J_g \frac{\partial W}{\partial \mathbf{F}_e} \mathbf{G}^{-T}$ [21, 22]. In addition, define $\mathbf{T}_k = \mathbf{T}|_{\overline{\Omega}_k}$, so $\mathbf{T}_1$, $\mathbf{T}_2$ and $\mathbf{T}_3$ are the first Piola Kirchoff stresses defined on the closure of Ω_1, Ω_2 and Ω_3 respectively. Then

$$
\begin{aligned}
E_1'[\mathbf{\Phi}]\mathbf{\Phi}' &= \sum_{k=1}^{3} \int_{\Omega_k} \underbrace{\mathbf{T}_k \mathbf{G}_k^{T}}_{\mathbf{A}^T} : \underbrace{(\nabla \mathbf{\Phi}')}_{\mathbf{B}} \underbrace{\mathbf{G}_k^{-1}}_{\mathbf{C}} dA \\
&= \sum_{k=1}^{3} \int_{\Omega} \mathbf{G}_k^{-1} (\mathbf{T}_k \mathbf{G}_k^{T})^{T} : (\nabla \mathbf{\Phi}')^{T} dA,
\end{aligned}
$$

using $\mathbf{A}^T : \mathbf{BC} = \mathbf{CA} : \mathbf{B}^T$ for any tensors $\mathbf{A}$, $\mathbf{B}$, $\mathbf{C}$. Therefore

$$
\begin{aligned}
E_1'[\mathbf{\Phi}]\mathbf{\Phi}' &= \sum_{k=1}^{3} \int_{\Omega_k} \mathbf{G}_k^{-1} \mathbf{G}_k \mathbf{T}_k^{T} : (\nabla \mathbf{\Phi}')^{T} dA \\
&= \sum_{k=1}^{3} \int_{\Omega_k} \mathbf{T}_k^{T} : (\nabla \mathbf{\Phi}')^{T} dA \\
&= \sum_{k=1}^{3} \int_{\Omega_k} \mathbf{T}_k : \nabla \mathbf{\Phi}' dA.
\end{aligned}
$$

- Gateaux derivative of E_2. Take $X \equiv X_1$, $Y \equiv X_2$, $Z \equiv X_3$, let $\mathrm{Cof}\mathbf{F} = J\mathbf{F}^{-T}$ be the cofactor matrix of $\mathbf{F}$ and let $\mathbf{N}$ be the outward normal on the reference boundary $\partial\Omega_1^{(1)}$. Then

$$
E_2[\mathbf{\Phi}] = \frac{P_1}{2} \int_{\partial\Omega_1^{(1)}} (\mathrm{Cof}\mathbf{F})\mathbf{N} \cdot \mathbf{\Phi} dS \tag{15}
$$

$$
= \frac{P_1}{4} \int_{\partial\Omega_1^{(1)}} \varepsilon_{mij} \varepsilon_{npq} \frac{\partial \Phi_m}{\partial X_n} \frac{\partial \Phi_i}{\partial X_p} \Phi_j N_q dS. \tag{16}
$$

7

For a second rank tensor $\mathbf{A}$ with entries

$$\mathbf{A} = \begin{pmatrix} A_{11} & A_{12} & 0 \\ A_{21} & A_{22} & 0 \\ 0 & 0 & 1 \end{pmatrix}, \tag{17}$$

and first rank tensors $\mathbf{N}$ and $\mathbf{B}$ with entries $\mathbf{N} = (N_1, N_2, 0)^T$, $\mathbf{B} = (B_1, B_2, B_3)^T$, we have the simplification

$$(\mathrm{Cof}\mathbf{A})\mathbf{N} \cdot \mathbf{B} = \frac{1}{2}\varepsilon_{mij}\varepsilon_{npq}A_{mn}A_{ip}B_jN_q = \varepsilon_{ij}\varepsilon_{pq}A_{ip}B_jN_q, \tag{18}$$

where the indices $i, j, m, n, p, q, \in \{1, 2, 3\}$ in the second term of (18), but $i, j, p, q \in \{1, 2\}$ in the final term. Since $\mathbf{F} = \nabla\boldsymbol{\Phi}$ in (15) has the sparsity structure (17), Eq. (16) implies

$$
\begin{aligned}
E_2[\boldsymbol{\Phi}] &= \frac{P_1}{2} \int_{\partial\Omega_1^{(1)}} \varepsilon_{ij}\varepsilon_{pq} \frac{\partial\Phi_i}{\partial X_p}\Phi_j N_q dS & (19)\\
\Rightarrow E_2'[\boldsymbol{\Phi}]\boldsymbol{\Phi}' &= \frac{P_1}{2} \int_{\partial\Omega_1^{(1)}} \varepsilon_{ij}\varepsilon_{pq} \left(\frac{\partial\Phi_i'}{\partial X_p}\Phi_j + \frac{\partial\Phi_i}{\partial X_p}\Phi_j' \right) N_q dS & (20)\\
&= \frac{P_1}{2} \int_{\partial\Omega_1^{(1)}} \varepsilon_{ij}\varepsilon_{pq} \left[\frac{\partial(\Phi_i'\Phi_j)}{\partial X_p} - \Phi_i'\frac{\partial\Phi_j}{\partial X_p} + \frac{\partial\Phi_i}{\partial X_p}\Phi_j' \right] N_q dS \\
&= \frac{P_1}{2} \int_{\partial\Omega_1^{(1)}} \varepsilon_{ij}\varepsilon_{pq} \frac{\partial(\Phi_i'\Phi_j)}{\partial X_p} N_q dS - \frac{P_1}{2} \int_{\partial\Omega_1^{(1)}} \varepsilon_{ij}\varepsilon_{pq} \left(\frac{\partial\Phi_j}{\partial X_p}\Phi_i' - \frac{\partial\Phi_i}{\partial X_p}\Phi_j' \right) N_q dS \\
&= \frac{P_1}{2} \int_{\partial\Omega_1^{(1)}} \varepsilon_{pq}N_q\frac{\partial}{\partial X_p}\left(\varepsilon_{ij}\Phi_i'\Phi_j \right) dS + P_1 \int_{\partial\Omega_1^{(1)}} \varepsilon_{ji}\varepsilon_{pq} \frac{\partial\Phi_j}{\partial X_p}\Phi_i' N_q dS.
\end{aligned}
$$

The first integral is zero because $\int_{\partial\Omega_1} \mathbf{N} \times \nabla f ds = \int_\Omega \nabla \times \nabla f dx = 0$ for any scalar f. Therefore

$$E_2'[\boldsymbol{\Phi}]\boldsymbol{\Phi}' = P_1 \int_{\partial\Omega_1^{(1)}} (\mathrm{Cof}\mathbf{F})\mathbf{N} \cdot \boldsymbol{\Phi}' dS, \tag{21}$$

again using (18). A similar calculation gives

$$E_3'[\boldsymbol{\Phi}]\boldsymbol{\Phi}' = P_2 \int_{\partial\Omega_3^{(2)}} (\mathrm{Cof}\mathbf{F})\mathbf{N} \cdot \boldsymbol{\Phi}' dS. \tag{22}$$

Assembling all the Gateaux derivatives:

$$
\Pi'[\boldsymbol{\Phi}]\boldsymbol{\Phi}' = \sum_{k=1}^{3}\int_{\Omega_k}\mathbf{T}_k : \nabla\boldsymbol{\Phi}'dA + P_1\int_{\partial\Omega_1^{(1)}}(\mathrm{Cof}\mathbf{F})\mathbf{N}\cdot\boldsymbol{\Phi}'dS + P_2\int_{\partial\Omega_3^{(2)}}(\mathrm{Cof}\mathbf{F})\mathbf{N}\cdot\boldsymbol{\Phi}'dS
$$

$$
= -\sum_{k=1}^{3}\int_{\Omega_k}(\nabla\cdot\mathbf{T}_k)\cdot\boldsymbol{\Phi}'dA
$$

$$
+ \int_{\partial\Omega_1^{(1)}}\mathbf{T}_1\mathbf{N}_1^{(1)}\cdot\boldsymbol{\Phi}'dS + \int_{\partial\Omega_1^{(2)}}\mathbf{T}_1\mathbf{N}_1^{(2)}\cdot\boldsymbol{\Phi}'dS
$$

$$
+ \int_{\partial\Omega_2^{(1)}}\mathbf{T}_2\mathbf{N}_2^{(1)}\cdot\boldsymbol{\Phi}'dS + \int_{\partial\Omega_2^{(2)}}\mathbf{T}_2\mathbf{N}_2^{(2)}\cdot\boldsymbol{\Phi}'dS
$$

$$
+ \int_{\partial\Omega_3^{(1)}}\mathbf{T}_3\mathbf{N}_3^{(1)}\cdot\boldsymbol{\Phi}'dS + \int_{\partial\Omega_3^{(2)}}\mathbf{T}_3\mathbf{N}_3^{(2)}\cdot\boldsymbol{\Phi}'dS
$$

$$
+ P_1\int_{\partial\Omega_1^{(1)}}(\mathrm{Cof}\mathbf{F})\mathbf{N}_1^{(1)}\cdot\boldsymbol{\Phi}'dS + P_2\int_{\partial\Omega_3^{(2)}}(\mathrm{Cof}\mathbf{F})\mathbf{N}_3^{(2)}\cdot\boldsymbol{\Phi}'dS.
$$

where we have used the divergence theorem on Ω_k, $k = 1,2,3$. We have also distinguished the normals on each boundary with $\mathbf{N}_i^{(j)}$ representing the outward normal on boundary $\partial\Omega_i^{(j)}$, with the consequence that $\mathbf{N}_1^{(2)} = -\mathbf{N}_2^{(1)}$ and $\mathbf{N}_2^{(2)} = -\mathbf{N}_3^{(1)}$. Since $\Pi'[\boldsymbol{\Phi}]\boldsymbol{\Phi}' = 0$,

$$
0 = -\sum_{k=1}^{3}\int_{\Omega_k}(\nabla\cdot\mathbf{T}_k)\cdot\boldsymbol{\Phi}'dx
$$

$$
+ \int_{\partial\Omega_1^{(1)}}\left[\mathbf{T}_1\mathbf{N}_1^{(1)} + P_1(\mathrm{Cof}\mathbf{F})\mathbf{N}_1^{(1)}\right]\cdot\boldsymbol{\Phi}'dS + \int_{\partial\Omega_3^{(2)}}\left[\mathbf{T}_3\mathbf{N}_3^{(2)} + P_2(\mathrm{Cof}\mathbf{F})\mathbf{N}_3^{(2)}\right]\cdot\boldsymbol{\Phi}'dS
$$

$$
+ \int_{\partial\Omega_1^{(2)}}(\mathbf{T}_1\mathbf{N}_1^{(2)} + \mathbf{T}_2\mathbf{N}_2^{(1)})\cdot\boldsymbol{\Phi}'dS + \int_{\partial\Omega_2^{(2)}}(\mathbf{T}_2\mathbf{N}_2^{(2)} + \mathbf{T}_3\mathbf{N}_3^{(1)})\cdot\boldsymbol{\Phi}'dS,
$$

for all sufficiently smooth test functions $\boldsymbol{\Phi}'$. Therefore the strong form boundary value problem is

$$
\begin{aligned}
\nabla\cdot\mathbf{T}_k &= 0, & (X,Y)\in\Omega_k, & \quad k = 1,2,3, \\
\mathbf{T}_1\mathbf{N}_1^{(1)} &= -P_1(\mathrm{Cof}\mathbf{F})\mathbf{N}_1^{(1)}, & (X,Y)\in\partial\Omega_1^{(1)} \\
\mathbf{T}_1\mathbf{N}_1^{(2)} &= \mathbf{T}_2\mathbf{N}_1^{(2)}, & (X,Y)\in\partial\Omega_1^{(2)}, \\
\mathbf{T}_2\mathbf{N}_2^{(2)} &= \mathbf{T}_3\mathbf{N}_2^{(2)}, & (X,Y)\in\partial\Omega_2^{(2)}, \\
\mathbf{T}_3\mathbf{N}_3^{(2)} &= -P_2(\mathrm{Cof}\mathbf{F})\mathbf{N}_3^{(2)}, & (X,Y)\in\partial\Omega_3^{(2)}.
\end{aligned}
$$

In terms of the deformed domain and Cauchy stress, these equations are

$$
\begin{aligned}
\nabla\cdot\boldsymbol{\sigma}_k &= 0, & (x,y)\in\omega_k, & \quad k = 1,2,3, & (23) \\
\boldsymbol{\sigma}_1\mathbf{n} &= -P_1\mathbf{n}, & (x,y)\in\partial\omega_1^{(1)} & & (24) \\
\boldsymbol{\sigma}_1\mathbf{n} &= \boldsymbol{\sigma}_2\mathbf{n}, & (x,y)\in\partial\omega_1^{(2)} & & (25) \\
\boldsymbol{\sigma}_2\mathbf{n} &= \boldsymbol{\sigma}_3\mathbf{n}, & (x,y)\in\partial\omega_2^{(2)} & & (26) \\
\boldsymbol{\sigma}_3\mathbf{n} &= -P_2\mathbf{n}, & (x,y)\in\partial\omega_3^{(2)}, & & (27)
\end{aligned}
$$

where $\boldsymbol{\sigma}_k$ is the Cauchy stress on $\omega_k = \boldsymbol{\Phi}(\Omega_k)$, $k = 1, 2, 3$; $\mathbf{n} = (n_1, n_2, 0)^T$ is the outward normal on interfaces of grown subdomains; and $\partial\omega_k^{(1)}$, $\partial\omega_k^{(2)}$ are the inner and outer boundaries of the deformed domain ω_k.

For our intimal thickening problem we assume no traction on $\partial\Omega_3^{(2)}$ so that $P_2 = 0$, and a given lumen pressure on $\partial\Omega_1^{(1)}$ so that $P_1 = P \geq 0$. Furthermore, since the intima grows much more quickly than the media and adventitia, we take

$$\mathbf{G}(X, Y) = \operatorname{diag}(g, g, 1), \qquad g(X, Y) = \left\{ \begin{array}{ll} g_0, & (X, Y) \in \Omega_1, \\ 1, & (X, Y) \in \Omega_2, \\ 1, & (X, Y) \in \Omega_3, \end{array} \right. \tag{28}$$

where g_0 is a given constant. If we write the work done by the lumen pressure in terms of the deformed, grown configuration but leave the volumetric energy in terms of the reference configuration, the energy functional that needs to be extremized is

$$\Pi = \sum_{k=1}^{3} \int_{\Omega_k} J_{g,k} \cdot W_k(\mathbf{F}_e) dA + \frac{P}{2} \int_{\partial\omega_1^{(1)}} \mathbf{n} \cdot \boldsymbol{\varphi} ds, \tag{29}$$

where $\mathbf{F}_e$ is the elastic part of the deformation gradient from eq. (1) and $\boldsymbol{\varphi} = (x, y, z)^T$ is the deformation field represented in the mapped domain.

3 Hyperelastic Strain Energy Density

We use a nearly-incompressible hyperelastic HGO strain energy function [3, 5] that penalizes deviations from from a unit elastic Jacobian:

$$W_k = \underbrace{\frac{\mu_k}{2}(I_1 - 3)}_{\substack{\text{energy of} \\ \text{ground substance}}} + \underbrace{\frac{\eta_k}{\beta_k} \left\{ e^{\beta_k \left[\rho_k (I_4 - 1)_+^2 + (1 - \rho_k)(I_1 - 3)^2 \right]} - 1 \right\}}_{\text{energy of collagen fibers, } W_{\text{fiber}}} + \underbrace{\frac{\nu\mu_k}{1 - 2\nu}(J_e - 1)^2 - \mu_k \ln J_e}_{\text{penalty and auxiliary terms}}, \tag{30}$$

for $k = 1$ (intima), $k = 2$ (media), and $k = 3$ (adventitia) so that μ_k is a (possibly different) constant within each arterial layer and likewise with η_k, β_k and ρ_k. Experimental values corresponding to a human coronary artery are given in Table 1. Furthermore, the strain energy only depends on the elastic Cauchy-Green deformation $\mathbf{C}_e$:

$$I_1 = \operatorname{Tr}(\mathbf{C}_e) = \operatorname{Tr}(\mathbf{F}_e^T \mathbf{F}_e) \tag{31}$$

$$I_4 = \mathbf{b}(X, Y)^T \mathbf{C}_e \mathbf{b}(X, Y), \tag{32}$$

$$J_e = \det \mathbf{F}_e, \tag{33}$$

where $\mathbf{b}$ is a pre-computed fiber direction vector: see below in section 3.1.

The purpose of the third term on the right hand side of (30) is to to penalize deformations that have J_e not equal to unity. When $\nu \approx 1/2$, this term penalizes deformations with $J \neq J_g$,

Symbol	Meaning	Value
μ_1	Intima shear modulus	27.9 kPa
η_1	Intima material parameter	263.66 kPa
β_1	Intima material parameter	170.88
ρ_1	Intima material parameter	0.51
φ_1	Fiber angle in intima	60.3^o
μ_2	Media shear modulus	1.27 kPa
η_2	Media material parameter	21.6 kPa
β_2	Media material parameter	8.21
ρ_2	Media material parameter	0.25
φ_2	Fiber angle in media	20.61^o
μ_3	Adventitia shear modulus	7.56 kPa
η_3	Adventitia material parameter	38.57 kPa
β_3	Adventitia material parameter	85.03
ρ_3	Adventitia material parameter	0.55
φ_3	Fiber angle in adventitia	67°

Table 1: Material parameters for the functional (30) taken from [3]

thereby ensuring that individual elements approximately grow (or shrink) by an amount given by the growth tensor. The auxiliary term $-\mu \ln J_e$ ensures that the stress in the undeformed configuration is zero: for more information on compressible versions of hyperelastic energies see [23]. The second term on the right hand side containing the exponential function describes the energy of collagen fibers [4, 5, 24] and renders the artery anisotropic. It contains several features that make continuum modeling of arteries unique. First is the presence of the collagen fibers. The orientation of these fibers is locally given by the unit vector $\mathbf{b}$; we show how to compute $\mathbf{b}$ in the next section. Second, these fibers only play a role when they are extended which is mathematically equivalent to $I_4 > 1$. This behavior justifies the notation

$$(I_4 - 1)_+^2 = \begin{cases} (I_4 - 1)^2, & \text{if } I_4 > 1, \\ 0, & \text{if } I_4 \leq 1. \end{cases} \tag{34}$$

The method we use in this paper is a "single-field" approach, based on finding the position fields that correspond to the stationary points of the functional (30). One well-known problem with these types of methods is that they are prone to "locking" when the material is nearly incompressible (ν is close to $1/2$). Nevertheless, we hope to gain some insight into morphoelastic arterial mechanics with our algorithm by using modest values of ν.

Note on polyconvexity of (30). The existence of at least one solution in hyperelasticity boundary value problems depends on the polyconvexity of the strain energy [19]. A strain energy of the form $W(X, Y, \mathbf{F}, \text{Cof } \mathbf{F}, \det \mathbf{F})$ is polyconvex in $\mathbf{F}$ if it is convex in $(\mathbf{F}, \text{Cof } \mathbf{F}, \det \mathbf{F})$ for "almost" all (X, Y). It can be shown [20] that physically reasonable strain energies cannot be convex when regarded purely as a function of $\mathbf{F}$, which naturally leads to the notion of polyconvexity.

One simple way of constructing polyconvex functions is to sum a convex function of $\mathbf{F}$, a convex function of Cof $\mathbf{F}$ and a convex function of det $\mathbf{F}$. It is straightforward to show using the theorems in [20] that with a growth tensor $\mathbf{G} = \mathrm{diag}(g, g, 1)$, $I_1 = \frac{\mu}{2}(\lambda_1^2/g^2 + \lambda_2^2/g^2 + \lambda_3^2 - 3)$ with $\lambda_1 > 0$, $\lambda_2 > 0$, $\lambda_3 = 1$ the square-roots of the eigenvalues of $\mathbf{F}^T\mathbf{F}$ with the conclusion that I_1 is convex in $\mathbf{F}$. The penalty term $\frac{\nu\mu}{1-2\nu}(J/g^2 - 1)^2 - \mu\ln(J/g^2)$ is convex in J since its second derivative is strictly positive for $J > 0$. When $\rho = 1$, convexity of W_{fiber} in the case with no growth ($I_4 = \mathbf{b}^T\mathbf{C}\mathbf{b}$) was proved in [25]. However, convexity in the case with growth is also easily proved because $I_4 = \mathbf{b}^T\mathbf{C}_e\mathbf{b} \implies I_4 = \widehat{\mathbf{b}}^T\mathbf{C}\widehat{\mathbf{b}}$ with a redefined fiber vector $\widehat{\mathbf{b}} = \mathbf{G}^{-1}\mathbf{b}$. The actual strain energy used in eq. (29) is of the form $J_g \cdot W(X, Y, \mathbf{F}\mathbf{G}^{-1})$ but the pre-factor J_g does not alter polyconvexity because in our model it is independent of $\mathbf{F}$. Therefore when $\rho = 1$, W is polyconvex. When $0 < \rho < 1$, polyconvexity of W is harder to establish and may not even hold for certain parameter values.

3.1   Model of Collagen Fibers
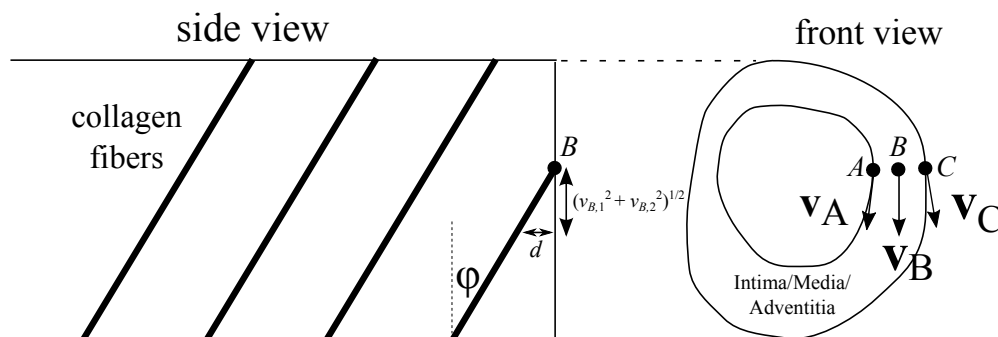
Figure 2: Orientation of a single family of fiber within the intima, media or adventitia (a representative layer is shown here). The vector $\mathbf{v}_B$ is calculated from tangent vectors at A and C (see eq. (36)). The (unscaled) fiber direction vector is computed as $(v_{B,1}, v_{B,2}, d)$ where $\tan\varphi = \frac{d}{\sqrt{v_{B,1}^2 + v_{B,2}^2}}$.

We now explain the form of the fiber energy in eq. (30). Embedded within the walls of the artery are two families of collagen fibers, which are oriented helically. When the arterial wall is undeformed, they are in a "crimped" configuration. Under large deformation these fibers unravel, become difficult to extend, and are responsible for anisotropy in the mechanical properties of the intima, media and adventitia. It is hypothesized that the presence of these fibers suppress positive remodeling [26]: as the layers are strained, they become stiffer and stiffer until further dilation of these outer layers is no longer energetically favorable.

To describe this effect, we assume that there are two smooth and continuous "fiber fields" $\mathbf{b}(X, Y, Z)$ and $\mathbf{b}^*(X, Y, Z)$ associated with the intima, media and adventitia and that at every point in the tissue (X, Y, Z), each fiber field is tangential to the corresponding set of collagen fibers passing through (X, Y, Z). The energy associated with elastically deforming

these fibers is represented using the Holzapfel-Gasser-Ogden model [24]:

$$W_{\text{fiber}} = \frac{\eta}{2\beta} \left(e^{\beta\left[\rho(I_4-1)_+^2 + (1-\rho)(I_1-3)^2\right]} - 1 \right) + \frac{\eta^*}{2\beta^*} \left(e^{\beta^*\left[\rho^*(I_4^*-1)_+^2 + (1-\rho^*)(I_1-3)^2\right]} - 1 \right), \quad (35)$$

where $I_4 = \mathbf{b}^T \mathbf{C}_e \mathbf{b}$, $I_4^* = \mathbf{b}^{*T} \mathbf{C}_e \mathbf{b}^*$ are the fiber lengths under the action of the elastic tensor and η, β, ρ, η^*, β^*, ρ^* are mechanical parameters (subscripts have been dropped for simplicity).

Consider one family of fibers, as shown in Figure 2 with fiber field $\mathbf{b}(X, Y, Z)$ where $\mathbf{b}$ is a unit vector. Now we describe how to compute $\mathbf{b}(X, Y, Z)$. Consider the vector $\mathbf{v}_B \in \mathbb{R}^2$, a projection of $\mathbf{b}$ onto the (X, Y) plane: see the "front view" of Figure 2. This vector is computed as a weighted average of tangent vectors on the inner ($\mathbf{v}_A$) and outer ($\mathbf{v}_C$) boundaries:

$$\mathbf{v}_B = \frac{|BC|\mathbf{v}_A + |AB|\mathbf{v}_C}{|BC| + |AB|}, \quad (36)$$

where A is the point on the inner boundary closest to B; C is the point on the outer boundary closest to B; $|AB|$ is the shortest distance between A and B; and $|BC|$ is the shortest distance between points B and C. In this paper we assume that the boundaries $\partial\Omega_k^{(1)}$, $k = 1, 2, 3$ are convex so that A is unique, given B. In addition, if B is within a radius of curvature of the outer boundary[1], then C is also unique; this second condition can be satisfied by ensuring that the intima, media and adventitia layers are sufficiently thin. When both conditions are satisfied, A and C can be found by dropping perpendiculars to the boundaries or by optimization. The closer the point B is to the inner boundary, the more weight is given to $\mathbf{v}_A$ and $\mathbf{v}_B$ is more aligned with $\mathbf{v}_A$. Similarly, the closer the point B is to the outer boundary, the more weight is given to $\mathbf{v}_C$ and $\mathbf{v}_B$ is more aligned with $\mathbf{v}_C$.

The full 3D unit fiber vector is found by inclining $\mathbf{v}_B \equiv (v_{B,1}, v_{B,2})$ in the Z-direction by an angle φ and normalizing so that $\mathbf{b}$ has unit length:

$$\mathbf{b} = \begin{pmatrix} b_1 \\ b_2 \\ b_3 \end{pmatrix} = \frac{\left(v_{B,1}, v_{B,2}, \sqrt{v_{B,1}^2 + v_{B,2}^2} \tan\varphi \right)}{\sqrt{(v_{B,1}^2 + v_{B,2}^2)(1 + \tan^2\varphi)}}. \quad (37)$$

Figure 3 shows that our method outputs fiber directions $\mathbf{v}_B$ that change smoothly throughout the three arterial layers.

The second family of fibers is inclined at an angle $\pi - \varphi$ rather than φ. The corresponding fiber field is identical to (37) but with $\tan\varphi$ replaced by $-\tan\varphi$, resulting in $\mathbf{b}^* = (b_1, b_2, -b_3)$ and $I_4 = I_4^*$. Moreover, if we assume that the mechanical properties of the second family are identical to the first, then $\eta = \eta^*$, $\beta = \beta^*$ and $\rho = \rho^*$ and from (35), the contributions from both sets of fibers is

$$W_{\text{fiber}} = \frac{\eta}{\beta} \left(e^{\beta\left[\rho(I_4-1)_+^2 + (1-\rho)(I_1-3)^2\right]} - 1 \right), \quad (38)$$

---

[1]Suppose the outer boundary is a closed, convex curve Γ. For every point $P \in \Gamma$, consider the center of the associated (and unique) osculating circle passing through P. Let Γ' be the locus of points traced out by the circle's center as P traverses Γ. If B lies in the region enclosed by Γ and Γ', then C is unique.

and $\beta = \beta_k$ for $k = 1$ (intima), $k = 2$ (media) and $k = 3$ (adventitia) and similarly with η and ρ. The angle of inclination φ is also assumed to be a (different) constant in every layer: $\varphi = \varphi_k$ for $k = 1$ (intima), $k = 2$ (media) and $k = 3$ (adventitia).
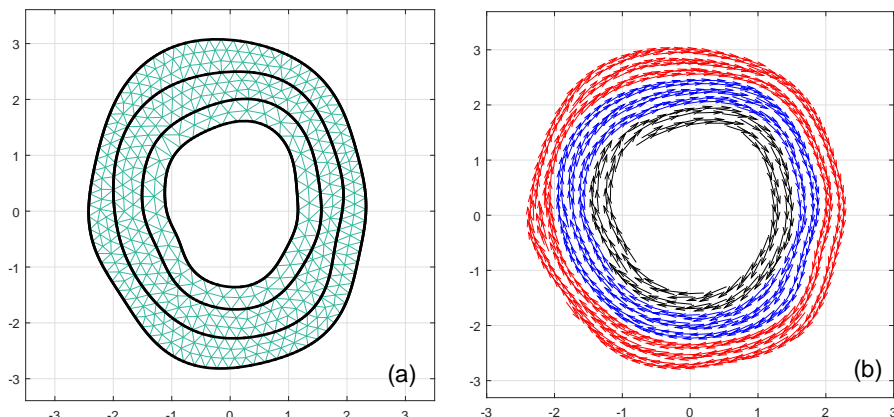
Figure 3: (a) Mesh used for finite element method, generated using `distmesh.m` [27]. (b) Fiber directions $\mathbf{v}_B$ in the media and adventitia computed using (36).

4 Implementation

4.1 Notation and Definitions

Using double index summation convention, the energy functional (29) along with (30) is discretized through the introduction of the standard piecewise linear nodal basis:

$$x = x_k \phi_k(X, Y), \qquad y = y_k \phi_k(X, Y). \tag{39}$$

Our convention is to use lower case symbols for variables relating to the deformed configuration and upper case letters for the reference configuration. For example, coordinates of nodes on the mesh are denoted (X_k, Y_k), $k = 1, \ldots, n$, and the discretized position field (essentially, the deformed node positions) is denoted (x_k, y_k), $k = 1, \ldots, n$ where n is the total number of vertices in the triangulation.

Consider a triangular element Q with associated nodes $Q(1)$, $Q(2)$ and $Q(3)$. Let $(X_{Q(i)}, Y_{Q(i)})$ be the coordinates of node $Q(i)$. On element Q, the nodal basis function $\phi_{Q(i)}(X, Y)$ is linear in X and Y:

$$\phi_{Q(i)}(X, Y) = A_{Q(i)} X + B_{Q(i)} Y + C_{Q(i)}, \qquad i = 1, 2, 3, \tag{40}$$

$$\Rightarrow A_{Q(i)} = \frac{\partial \phi_{Q(i)}}{\partial X}, \qquad B_{Q(i)} = \frac{\partial \phi_{Q(i)}}{\partial Y}. \tag{41}$$

14

Since $\phi_{Q(1)}(X_{Q(1)}, Y_{Q(1)}) = 1$, but $\phi_{Q(1)}(X_{Q(2)}, Y_{Q(2)}) = 0$ and $\phi_{Q(1)}(X_{Q(3)}, Y_{Q(3)}) = 0$,

$$\begin{bmatrix} X_{Q(1)} & Y_{Q(1)} & 1 \\ X_{Q(2)} & Y_{Q(2)} & 1 \\ X_{Q(3)} & Y_{Q(3)} & 1 \end{bmatrix} \begin{bmatrix} A_{Q(1)} \\ B_{Q(1)} \\ C_{Q(1)} \end{bmatrix} = \begin{bmatrix} 1 \\ 0 \\ 0 \end{bmatrix}.$$

The same principle can be applied to $\phi_{Q(2)}$ and $\phi_{Q(3)}$ so have the standard inversion to find basis coefficients:

$$\begin{bmatrix} X_{Q(1)} & Y_{Q(1)} & 1 \\ X_{Q(2)} & Y_{Q(2)} & 1 \\ X_{Q(3)} & Y_{Q(3)} & 1 \end{bmatrix} \begin{bmatrix} A_{Q(1)} & A_{Q(2)} & A_{Q(3)} \\ B_{Q(1)} & B_{Q(2)} & B_{Q(3)} \\ C_{Q(1)} & C_{Q(2)} & C_{Q(3)} \end{bmatrix} = \begin{bmatrix} 1 & 0 & 0 \\ 0 & 1 & 0 \\ 0 & 0 & 1 \end{bmatrix}. \tag{42}$$

The method we present uses several matrices that are produced by various combinations of derivatives of basis functions and fiber directions (b_1, b_2, b_3). For example, the $n \times n$ matrices $\mathbf{U}$, $\mathbf{N}$, $\mathbf{H}$, and $\mathbf{L}$ appear several times and their entries are

$$U_{jr} = \frac{\partial \phi_j}{\partial X} \frac{\partial \phi_r}{\partial X} + \frac{\partial \phi_j}{\partial Y} \frac{\partial \phi_r}{\partial Y}, \tag{43}$$

$$N_{jr} = \frac{\partial \phi_j}{\partial X} \frac{\partial \phi_r}{\partial Y} - \frac{\partial \phi_j}{\partial Y} \frac{\partial \phi_r}{\partial X}, \tag{44}$$

$$H_{jr} = b_1^2 \frac{\partial \phi_j}{\partial X} \frac{\partial \phi_r}{\partial X} + 2b_1 b_2 \frac{\partial \phi_j}{\partial X} \frac{\partial \phi_r}{\partial Y} + b_2^2 \frac{\partial \phi_j}{\partial Y} \frac{\partial \phi_r}{\partial Y}, \tag{45}$$

$$L_{jr} = b_1^2 \frac{\partial \phi_j}{\partial X} \frac{\partial \phi_r}{\partial X} + b_1 b_2 \left(\frac{\partial \phi_j}{\partial X} \frac{\partial \phi_r}{\partial Y} + \frac{\partial \phi_j}{\partial Y} \frac{\partial \phi_r}{\partial X} \right) + b_2^2 \frac{\partial \phi_j}{\partial Y} \frac{\partial \phi_r}{\partial Y}. \tag{46}$$

Sparse $n \times n$ elemental matrices (usually with only 9 non-zero elements) are given the tilde accent. For example the matrix $\mathbf{U}$ is built from repeated updates using $\tilde{\mathbf{U}}$ which we represent by $\mathbf{U} \leftarrow \mathbf{U} + \tilde{\mathbf{U}}$, looped over all elements. When writing the elemental equivalents of $\mathbf{N}$, $\mathbf{H}$, $\mathbf{U}$ and $\mathbf{L}$, we can always replace the derivatives of ϕ_k with A_k and B_k using eq. (41):

$$\tilde{U}_{jr} = A_j A_r + B_j B_r, \tag{47}$$
$$\tilde{N}_{jr} = A_j B_r - B_j A_r, \tag{48}$$
$$\tilde{H}_{jr} = b_1^2 A_j A_r + 2b_1 b_2 A_j B_r + b_2^2 B_j B_r, \tag{49}$$
$$\tilde{L}_{jr} = b_1^2 A_j A_r + b_1 b_2 (A_j B_r + B_j A_r) + b_2^2 B_j B_r. \tag{50}$$

For reference it is also useful to have the expressions

$$
\mathbf{F}_e \;=\; \begin{bmatrix} \dfrac{x_i}{g}\dfrac{\partial \phi_i}{\partial X} & \dfrac{x_i}{g}\dfrac{\partial \phi_i}{\partial Y} & 0 \\[2ex] \dfrac{y_i}{g}\dfrac{\partial \phi_i}{\partial X} & \dfrac{y_i}{g}\dfrac{\partial \phi_i}{\partial Y} & 0 \\[2ex] 0 & 0 & 1 \end{bmatrix},
$$

$$
I_1 \;=\; \mathrm{Tr}(\mathbf{C}_e) = \frac{U_{ij}}{g^2}\,(x_i x_j + y_i y_j) + 1, \tag{51}
$$

$$
I_4 \;=\; \mathbf{b}^T \mathbf{C}_e \mathbf{b} = \frac{H_{ij}}{g^2}(x_i x_j + y_i y_j) + b_3^2, \tag{52}
$$

where we have used the growth law (28). Now, we give all the details of our numerical method. In section 4.2, we describe how to set up the individual matrices that make up the system of nonlinear algebraic equations which are solved to give the position fields. In section 4.3, we explain how to find the minimum-norm solution based on the QR factorization and finally in section 4.4 we explain how we compute the Cauchy stress from the elastic part of the deformation gradient.

4.2 Stationary Points of the Energy and Newton's Method

We now find the position fields that solve the equations of mechanical equilibrium (23)-(27) with $P_1 = P$ and $P_2 = 0$. From eqs. (29) and (30), our finite element method is based on finding the stationary points of the functional

$$
\begin{aligned}
\Pi \;=\; & \underbrace{\frac{1}{2}\int_\Omega J_g \cdot \mu (I_1 - 3)dA}_{\Pi_0} + \underbrace{\int_\Omega \frac{J_g \cdot \eta}{\beta}\left\{ e^{\beta\left[\rho(I_4-1)_+^2 + (1-\rho)(I_1-3)^2\right]} - 1 \right\}dA}_{\Pi_1} \\[2ex]
& + \frac{\nu}{1-2\nu}\underbrace{\int_\Omega J_g \cdot \mu (J_e - 1)^2 dA}_{\Pi_2} - \underbrace{\int_\Omega J_g \cdot \mu \ln J_e dA}_{\Pi_3} + \frac{P}{2}\underbrace{\int_{\partial \omega_1^{(1)}} \mathbf{n}\cdot\boldsymbol{\varphi}ds}_{\Pi_4}, \tag{53}
\end{aligned}
$$

over all continuous position fields $x(X,Y)$ and $y(X,Y)$ where $\mu = \mu_k$ for $k = 1$ (intima), $k = 2$ (media), and $k = 3$ (adventitia) so that μ_k is a (possibly different) constant within each arterial layer and likewise with η_k, β_k and ρ_k. Upon introducing the nodal basis (39), these fields are discretized resulting in $\mathbf{x} = (x_1, \ldots, x_n)^T$, and $\mathbf{y} = (y_1, \ldots, y_n)^T$. Hence we have $2n$ unknowns in total. Later, it will be convenient to refer to all node positions in a single vector: $\mathbf{z} = (x_1, \ldots, x_n, y_1, \ldots, y_n)^T$. The reference mesh positions are denoted $\mathbf{X}$ and $\mathbf{Y}$.

A stationary point of (53) can be found by direct differentiation. Upon applying the

gradient operator ∇ in $\mathbf{x}$ and $\mathbf{y}$, we have

$$\nabla_{\mathbf{x}}\Pi = \nabla_{\mathbf{x}}\left[\Pi_0 + \Pi_1 + \frac{\nu}{1-2\nu}\Pi_2 + \Pi_3 + \Pi_4\right] = \mathbf{0}, \tag{54}$$

$$\nabla_{\mathbf{y}}\Pi = \nabla_{\mathbf{y}}\left[\Pi_0 + \Pi_1 + \frac{\nu}{1-2\nu}\Pi_2 + \Pi_3 + \Pi_4\right] = \mathbf{0}, \tag{55}$$

which (as we will show) yields the following non-linear system of algebraic equations

$$\mathbf{Mx} + \mathbf{R}(\mathbf{x},\mathbf{y})\mathbf{x} + \frac{2\nu}{1-2\nu}\left(\mathbf{S}(\mathbf{x},\mathbf{y}) - \mathbf{E}\right)\mathbf{y} - \mathbf{V}(\mathbf{x},\mathbf{y})\mathbf{y} - \frac{P\mathbf{D}}{2}\mathbf{y} = \mathbf{0}, \tag{56}$$

$$\mathbf{My} + \mathbf{R}(\mathbf{x},\mathbf{y})\mathbf{y} - \frac{2\nu}{1-2\nu}\left(\mathbf{S}(\mathbf{x},\mathbf{y}) - \mathbf{E}\right)\mathbf{x} + \mathbf{V}(\mathbf{x},\mathbf{y})\mathbf{x} + \frac{P\mathbf{D}}{2}\mathbf{x} = \mathbf{0}. \tag{57}$$

The matrices $\mathbf{M}$, $\mathbf{E}$ and $\mathbf{D}$ are constant with respect to $\mathbf{x}$, $\mathbf{y}$ and $\mathbf{S}$, $\mathbf{E}$, $\mathbf{V}$ and $\mathbf{D}$ are all skew-symmetric. We define all these matrices and explain how to construct them in the following subsections. Note that the discretization of Π_2 results in a '2' prefactor that multiplies the Poisson ratio in (56) and (57).

The nonlinear system of equations (56), (57) can be solved using the Newton-Raphson method. We rewrite this system as

$$\mathbf{f}(\mathbf{z}) = \mathbf{F}(\mathbf{z})\mathbf{z} = \mathbf{0}, \tag{58}$$

where

$$\mathbf{F}(\mathbf{z}) = \left[\begin{array}{cc} \mathbf{M} + \mathbf{R}(\mathbf{x},\mathbf{y}) & \mathbf{\Gamma}(\mathbf{x},\mathbf{y}) \\ -\mathbf{\Gamma}(\mathbf{x},\mathbf{y}) & \mathbf{M} + \mathbf{R}(\mathbf{x},\mathbf{y}) \end{array}\right] \in \mathbb{R}^{2n \times 2n}, \tag{59}$$

and

$$\mathbf{\Gamma} = \frac{2\nu}{1-2\nu}(\mathbf{S} - \mathbf{E}) - \mathbf{V} - \frac{P\mathbf{D}}{2} \in \mathbb{R}^{n \times n}. \tag{60}$$

To implement the Newton-Raphson method, we need $\mathbf{J}$, the Jacobian of $\mathbf{f}$, and this can be found by direct differentiation. Leveraging the structure of $\mathbf{f}$, we find that $\mathbf{J} = \mathbf{K} + \mathbf{F}$ where

$$\mathbf{K} = \left[\frac{\partial \mathbf{F}}{\partial z_1}\mathbf{z} \quad \frac{\partial \mathbf{F}}{\partial z_2}\mathbf{z} \quad \cdots \quad \frac{\partial \mathbf{F}}{\partial z_{2n}}\mathbf{z}\right], \qquad \frac{\partial \mathbf{F}}{\partial z_k} = \left[\begin{array}{cc} \frac{\partial \mathbf{R}}{\partial z_k} & \frac{\partial \mathbf{\Gamma}}{\partial z_k} \\ -\frac{\partial \mathbf{\Gamma}}{\partial z_k} & \frac{\partial \mathbf{R}}{\partial z_k} \end{array}\right], \tag{61}$$

$k = 1, 2, \ldots, 2n$ and we show how to build $\mathbf{K}$ from submatrices in Appendix A.1. The Newton-Raphson method is then implemented as

$$[\mathbf{J}(\mathbf{z}_i)]\,\delta\mathbf{z} = [\mathbf{K}(\mathbf{z}_i) + \mathbf{F}(\mathbf{z}_i)]\,\delta\mathbf{z} = -\mathbf{f}(\mathbf{z}_i), \tag{62}$$

$$\mathbf{z}_{i+1} = \mathbf{z}_i + \delta\mathbf{z}, \tag{63}$$

where $\mathbf{z}_i$ is the ith iteration of the position field.

Generally, we find $\mathbf{J}$ to be singular with the consequence that the solution for $\delta\mathbf{z}$ is not unique. This is because the $\mathbf{x}$ and $\mathbf{y}$ that make (53) stationary are not unique: for example,

17

rigid body transformations (RBTs) of a minimizing position field are also solutions. To re-solve the multiplicity caused by RBTs, we compute the minimum norm solution of (62): see section 4.3. There may also be minimizers of (53) that are not related by RBTs. In theory, these could be found by initializing the Newton iteration with different initial guesses. High level pseudocode for implementing our method is given below:

Inputs: material parameters, reference mesh positions $\mathbf{X}$, $\mathbf{Y}$, lumen pressure $P \geq 0$ and a growth increment $\Delta g_0^{(k)}$ (recall that we are using the growth law (28)):

1. Set $g_0 = 1$. Take $k = 1$.

2. Take $\mathbf{x}_k = \mathbf{X}$ and $\mathbf{y}_k = \mathbf{Y}$ as initial conditions to solve (56) and (57) using the Newton-Raphson Method. The result is $(\mathbf{x}_{k+1}, \mathbf{y}_{k+1})$.

3. $k \to k + 1$, $g_0 \to g_0 + \Delta g_0^{(k)}$.

4. Go to step 2.

A good initial guess for Newton's method is crucial to its convergence. The node positions for the problem with growth g_0 provide the guess for the problem with growth $g_0 + \Delta g_0^{(k)}$.

When P is large, the reference frame positions $(\mathbf{X}, \mathbf{Y})$ provide a poor approximation to the true solution even when $g_0 = 1$. In this case, we also increase the pressure in small increments ΔP (keeping $g_0 = 1$) and find deformed node positions after each increment. When the solution for $(P > 0, g_0 = 1)$ is obtained, g_0 is slowly increased to its final desired value following the pseudo-code above.

4.2.1 Construction of M

Consider the integral

$$\Pi_0 = \int_\Omega \frac{\mu g^2}{2}(I_1 - 3)dXdY. \tag{64}$$

Upon introducing the nodal basis functions (39), we have

$$\frac{\partial \Pi_0}{\partial x_j} = x_k \int_\Omega \mu(X,Y) \left(\frac{\partial \phi_k}{\partial X} \frac{\partial \phi_j}{\partial X} + \frac{\partial \phi_k}{\partial Y} \frac{\partial \phi_j}{\partial Y} \right) dXdY \equiv x_k M_{kj} \tag{65}$$

$$\frac{\partial \Pi_0}{\partial y_j} = y_k \int_\Omega \mu(X,Y) \left(\frac{\partial \phi_k}{\partial X} \frac{\partial \phi_j}{\partial X} + \frac{\partial \phi_k}{\partial Y} \frac{\partial \phi_j}{\partial Y} \right) dXdY \equiv y_k M_{kj}, \tag{66}$$

where

$$M_{kj} = \int_\Omega \mu(X,Y) \left(\frac{\partial \phi_k}{\partial X} \frac{\partial \phi_j}{\partial X} + \frac{\partial \phi_k}{\partial Y} \frac{\partial \phi_j}{\partial Y} \right) dXdY. \tag{67}$$

The large matrix $\mathbf{M}$ is constructed by repeated updates using an elemental matrix $\tilde{M}_{Q(i),Q(j)}$, $i, j = 1, 2, 3$, that corresponds to the three vertices $Q(1)$, $Q(2)$ and $Q(3)$:

$$\tilde{M}_{Q(i),Q(j)} = \Delta_Q \mu_Q \tilde{U}_{Q(i),Q(j)}, \qquad i, j = 1, 2, 3, \tag{68}$$

18

where $\tilde{U}_{jr}$ is defined in (47) and Δ_Q is the area of the element:

$$\Delta_Q = \frac{(X_{Q(2)} - X_{Q(1)})(Y_{Q(3)} - Y_{Q(1)}) - (X_{Q(3)} - X_{Q(1)})(Y_{Q(2)} - Y_{Q(1)})}{2}, \tag{69}$$

and μ_Q is the value of μ on element Q (a similar convention is adopted for p_Q given any spatially-varying quantity p). Since the elemental matrices $\tilde{\mathbf{M}}$ are symmetric, $\mathbf{M} = \mathbf{M}^T$.

In summary,

$$\boxed{\nabla_{\mathbf{x}}\Pi_0 = \mathbf{Mx}, \qquad \nabla_{\mathbf{y}}\Pi_0 = \mathbf{My}.} \tag{70}$$

To build $\mathbf{M}$, one cycles through each element in the mesh and updates $\mathbf{M} \leftarrow \mathbf{M} + \tilde{\mathbf{M}}$.

4.2.2 Construction of $\mathbf{R}(\mathbf{x}, \mathbf{y})$

First we give some useful preliminary results. The derivatives of the Cauchy-Green tensor are

$$\frac{\partial \mathbf{C}_e}{\partial x_j} = \begin{bmatrix} \frac{2}{g^2}\left(\frac{\partial \phi_j}{\partial X}\frac{\partial \phi_r}{\partial X}\right)x_r & \frac{1}{g^2}\left(\frac{\partial \phi_j}{\partial X}\frac{\partial \phi_r}{\partial Y} + \frac{\partial \phi_j}{\partial Y}\frac{\partial \phi_r}{\partial X}\right)x_r & 0 \\ \frac{1}{g^2}\left(\frac{\partial \phi_j}{\partial X}\frac{\partial \phi_r}{\partial Y} + \frac{\partial \phi_j}{\partial Y}\frac{\partial \phi_r}{\partial X}\right)x_r & \frac{2}{g^2}\left(\frac{\partial \phi_j}{\partial Y}\frac{\partial \phi_r}{\partial Y}\right)x_r & 0 \\ 0 & 0 & 0 \end{bmatrix},$$

$$\frac{\partial \mathbf{C}_e}{\partial y_j} = \begin{bmatrix} \frac{2}{g^2}\left(\frac{\partial \phi_j}{\partial X}\frac{\partial \phi_r}{\partial X}\right)y_r & \frac{1}{g^2}\left(\frac{\partial \phi_j}{\partial X}\frac{\partial \phi_r}{\partial Y} + \frac{\partial \phi_j}{\partial Y}\frac{\partial \phi_r}{\partial X}\right)y_r & 0 \\ \frac{1}{g^2}\left(\frac{\partial \phi_j}{\partial X}\frac{\partial \phi_r}{\partial Y} + \frac{\partial \phi_j}{\partial Y}\frac{\partial \phi_r}{\partial X}\right)y_r & \frac{2}{g^2}\left(\frac{\partial \phi_j}{\partial Y}\frac{\partial \phi_r}{\partial Y}\right)y_r & 0 \\ 0 & 0 & 0 \end{bmatrix},$$

and for reference,

$$\frac{\partial I_4}{\partial \mathbf{C}_e} = \begin{bmatrix} b_1^2 & b_1 b_2 & b_1 b_3 \\ b_2 b_1 & b_2^2 & b_2 b_3 \\ b_3 b_1 & b_3 b_2 & b_3^2 \end{bmatrix} = \mathbf{b} \otimes \mathbf{b},$$

$$[\mathbf{b} \otimes \mathbf{b}] : \frac{\partial \mathbf{C}_e}{\partial x_j} = \frac{2}{g^2}L_{jr}x_r,$$

$$[\mathbf{b} \otimes \mathbf{b}] : \frac{\partial \mathbf{C}_e}{\partial y_j} = \frac{2}{g^2}L_{jr}y_r,$$

$$\mathbf{I} : \frac{\partial \mathbf{C}_e}{\partial x_j} = \frac{2}{g^2}U_{jr}x_r,$$

$$\mathbf{I} : \frac{\partial \mathbf{C}_e}{\partial y_j} = \frac{2}{g^2}U_{jr}y_r,$$

where the definition of I_4 is given in (52) and L_{jr} and U_{jr} are defined by eqs. (46) and (43). The double dot product for matrices $\mathbf{A}$ and $\mathbf{B}$ is $\mathbf{A} : \mathbf{B} = \sum_i \sum_j A_{ij} B_{ij}$.

19

Consider the integral

$$\Pi_1 = \int_\Omega g^2 \cdot W_{\text{fiber}} \, dA = \int_\Omega \frac{\eta g^2}{\beta} \left\{ e^{\beta \left[\rho (I_4 - 1)_+^2 + (1-\rho)(I_1 - 3)^2 \right]} - 1 \right\} dA,$$

where $\eta = \eta(X, Y)$, $\beta = \beta(X, Y)$. The **x**-gradient is

$$
\begin{aligned}
\frac{\partial \Pi_1}{\partial x_j} &= \int_\Omega g^2 \frac{\partial W_{\text{fiber}}}{\partial I_4} \left(\frac{\partial I_4}{\partial \mathbf{C}_e} : \frac{\partial \mathbf{C}_e}{\partial x_j} \right) + g^2 \frac{\partial W_{\text{fiber}}}{\partial I_1} \left(\frac{\partial I_1}{\partial \mathbf{C}_e} : \frac{\partial \mathbf{C}_e}{\partial x_j} \right) dA, \\
&= 2 \int_\Omega \eta g^2 \rho (I_4 - 1)_+ e^{\beta \left[\rho(I_4-1)_+^2 + (1-\rho)(I_1-3)^2 \right]} \left[\mathbf{b} \otimes \mathbf{b} \right] : \frac{\partial \mathbf{C}_e}{\partial x_j} dA + \\
&\quad\; 2 \int_\Omega \eta g^2 (1-\rho)(I_1 - 3) e^{\beta \left[\rho(I_4-1)_+^2 + (1-\rho)(I_1-3)^2 \right]} \mathbf{I} : \frac{\partial \mathbf{C}_e}{\partial x_j} dA, \\
&\equiv R_{jr} x_r, \tag{71}
\end{aligned}
$$

and similarly, the **y**-gradient is $\dfrac{\partial \Pi_1}{\partial y_j} = R_{jr} y_r$, where

$$R_{jr} = 4 \int_\Omega \eta e^{\beta(\rho \lambda_+^2 + (1-\rho)\sigma^2)} [\rho \lambda_+ L_{jr} + (1-\rho)\sigma U_{jr}] dA, \tag{72}$$

and $\sigma = I_1 - 3$, $\lambda = I_4 - 1$ are discretized through eqs. (51),(52). In summary, the matrix **R** results from taking the gradient of Π_1:

$$\boxed{\nabla_{\mathbf{x}} \Pi_1 = \mathbf{Rx}, \qquad \nabla_{\mathbf{y}} \Pi_1 = \mathbf{Ry},} \tag{73}$$

and **R** is constructed from elemental submatrices $\tilde{\mathbf{R}}$:

$$
\begin{aligned}
\tilde{R}_{Q(i),Q(j)} &= 4 \Delta_Q \eta_Q \exp \left(\beta_Q \rho_Q (\lambda_Q)_+^2 + \beta_Q (1 - \rho_Q) \sigma_Q^2 \right) \left(\rho_Q (\lambda_Q)_+ \tilde{L}_{Q(i),Q(j)} + (1 - \rho_Q) \sigma_Q \tilde{U}_{Q(i),Q(j)} \right), \\
\lambda_Q &= \frac{1}{g_Q^2} \left(\mathbf{x}_Q^T \tilde{\mathbf{H}} \mathbf{x}_Q + \mathbf{y}_Q^T \tilde{\mathbf{H}} \mathbf{y}_Q \right) + b_{3,Q}^2 - 1, \tag{74} \\
\sigma_Q &= \frac{1}{g_Q^2} \left(\mathbf{x}_Q^T \tilde{\mathbf{U}} \mathbf{x}_Q + \mathbf{y}_Q^T \tilde{\mathbf{U}} \mathbf{y}_Q \right) - 2, \tag{75}
\end{aligned}
$$

with $\tilde{L}_{jr}$, $\tilde{H}_{jr}$ and $\tilde{U}_{jr}$ defined in (50), (49) and (47) and $x_+ \equiv \max(0, x)$.

4.2.3 Construction of S(x, y) and E

Consider the integral

$$\Pi_2 = \int_\Omega \mu g^2 (J_e - 1)^2 dA. \tag{76}$$

Then

$$\begin{aligned}
\frac{\partial \Pi_2}{\partial x_j} &= \frac{\partial}{\partial x_j} \int_\Omega \mu g^2 (J_e - 1)^2 dA \\
&= 2 \int_\Omega \left[\frac{x_k y_m N_{km}(X,Y)}{g^2} - 1 \right] \frac{N_{js}(X,Y) y_s}{g^2} \mu(X,Y) g^2(X,Y) dX dY, \\
&= 2 \int_\Omega \left(\frac{x_k N_{km} y_m}{g^2} \right) N_{js} y_s \mu dX dY - 2 \int_\Omega \mu N_{js} y_s dX dY, \\
&= 2 S_{js} y_s - 2 E_{js} y_s,
\end{aligned}$$

where N_{km} is defined in eq. (44) and

$$S_{js} = \int_\Omega \frac{(x_k N_{km} y_m) N_{js} \mu(X,Y)}{g^2} dX dY, \tag{77}$$

$$E_{js} = \int_\Omega N_{js} \mu(X,Y) dX dY. \tag{78}$$

Note that since N_{km} is skew symmetric, so are S_{js} and E_{js}: $S_{js} = -S_{sj}$ and $E_{js} = -E_{sj}$. Similarly,

$$\begin{aligned}
\frac{\partial \Pi_2}{\partial y_j} &= 2 \int_\Omega \frac{(x_k N_{km} y_m) N_{ij} x_i \mu}{g^2} dX dY - 2 \int_\Omega \mu N_{ij} x_i dX dY, \\
&= -2 S_{ji} x_i + 2 E_{ji} x_i.
\end{aligned}$$

In summary,

$$\boxed{\nabla_{\mathbf{x}} \Pi_2 = 2(\mathbf{S} - \mathbf{E})\mathbf{y}, \qquad \nabla_{\mathbf{y}} \Pi_2 = -2(\mathbf{S} - \mathbf{E})\mathbf{x},} \tag{79}$$

where the matrices $\mathbf{E}$ and $\mathbf{S}$ are constructed using elemental matrices $\tilde{\mathbf{E}}$ and $\tilde{\mathbf{S}}$:

$$\begin{aligned}
\tilde{E}_{Q(i),Q(j)} &= \Delta_Q \mu_Q \tilde{N}_{Q(i),Q(j)}. \\
\tilde{S}_{Q(i),Q(j)} &= \frac{\Delta_Q \mu_Q}{g_Q^2} \left(x_{Q(r)} \tilde{N}_{Q(r),Q(s)} y_{Q(s)} \right) \tilde{N}_{Q(i),Q(j)},
\end{aligned}$$

and $\tilde{N}_{jr}$ is defined in (48).

4.2.4 Construction of $\mathbf{V}(\mathbf{x}, \mathbf{y})$

Consider the integral

$$\Pi_3 = -\int_\Omega \mu(X,Y) g^2(X,Y) \ln J_e dA. \tag{80}$$

Then

$$\frac{\partial \Pi_3}{\partial x_j} = -\frac{\partial}{\partial x_j} \int_\Omega \mu g^2 \ln \left(\frac{x_k N_{km} y_m}{g^2} \right) dX dY, \tag{81}$$

$$= -y_m \underbrace{\int_\Omega \frac{g^2 N_{jm}}{x_k N_{km} y_m} \mu dX dY}_{V_{jm}}, \tag{82}$$

and similarly,

$$\frac{\partial \Pi_3}{\partial y_j} = -\frac{\partial}{\partial y_j} \int_\Omega \mu g^2 \ln J_e \, dX dY = -x_k V_{kj}. \tag{83}$$

In summary,

$$\boxed{\nabla_{\mathbf{x}}\Pi_3 = -\mathbf{V}(\mathbf{x}, \mathbf{y})\mathbf{y}, \qquad \nabla_{\mathbf{y}}\Pi_3 = -\mathbf{V}^T(\mathbf{x}, \mathbf{y})\mathbf{x} = \mathbf{V}(\mathbf{x}, \mathbf{y})\mathbf{x},} \tag{84}$$

where the skew-symmetric matrix $\mathbf{V}$ is constructed from the elemental matrices $\tilde{\mathbf{V}}$:

$$\tilde{V}_{Q(i),Q(j)} = \frac{\Delta_Q \mu_Q g_Q^2 \tilde{N}_{Q(i),Q(j)}}{x_{Q(r)} y_{Q(s)} \tilde{N}_{Q(r),Q(s)}}, \tag{85}$$

4.2.5 Construction of D

Suppose that the N points $(x_{b(k)}, y_{b(k)})$, $k = 1, \ldots N$ lie on the the boundary $\partial \omega_1^{(1)}$. Since $\partial \omega_1^{(1)}$ is a closed curve, arithmetic on the indices of these nodes is performed modulo N in this section, e.g. $x_{b(N+1)} = x_{b(1)}$. Consider the boundary term

$$\Pi_4 = \frac{P}{2} \int_{\partial \omega_1^{(1)}} \mathbf{n} \cdot \boldsymbol{\varphi} ds \approx \frac{P}{2} \sum_{k=1}^{N} \mathbf{n}_{b(k)} \cdot \boldsymbol{\varphi}_{b(k)} \delta s_{b(k)}, \tag{86}$$

where $\partial \omega_1^{(1)}$ is traversed anti-clockwise and the deformed line element is

$$\delta s_{b(k)} = \sqrt{(x_{b(k+1)} - x_{b(k)})^2 + (y_{b(k+1)} - y_{b(k)})^2}, \qquad k = 1, \ldots, N. \tag{87}$$

We consider the deformation of the midpoint of line elements $\delta s_{b(k)}$ with unit normals

$$\mathbf{n}_{b(k)} = \frac{(y_{b(k)} - y_{b(k+1)}, x_{b(k+1)} - x_{b(k)})^T}{\delta s_{b(k)}}, \qquad k = 1, \ldots, N, \tag{88}$$

so that $\nabla_{\mathbf{z}}\Pi_4$ is discretized as

$$\begin{aligned}
\frac{\partial \Pi_4}{\partial x_j} &= \frac{P}{4} \frac{\partial}{\partial x_j} \sum_{k=1}^{N} \begin{pmatrix} y_{b(k)} - y_{b(k+1)} \\ x_{b(k+1)} - x_{b(k)} \end{pmatrix} \cdot \begin{pmatrix} x_{b(k)} + x_{b(k+1)} \\ y_{b(k)} + y_{b(k+1)} \end{pmatrix} \\
&= \frac{P}{4} \frac{\partial}{\partial x_j} \sum_{k=1}^{N} (x_{b(k)} + x_{b(k+1)})(y_{b(k)} - y_{b(k+1)}) + (x_{b(k+1)} - x_{b(k)})(y_{b(k)} + y_{b(k+1)}), \\
&= \frac{P}{4} \sum_{k=1}^{N} (\delta_{j,b(k)} + \delta_{j,b(k+1)})(y_{b(k)} - y_{b(k+1)}) + (\delta_{j,b(k+1)} - \delta_{j,b(k)})(y_{b(k)} + y_{b(k+1)}), \\
&= \frac{P}{4} [(y_j - y_{j+}) + (y_{j-} - y_j) + (y_{j-} + y_j) - (y_j + y_{j+})], \\
&= -\frac{P}{2}(y_{j+} - y_{j-}).
\end{aligned}$$

Similarly,

$$
\begin{aligned}
\frac{\partial \Pi_4}{\partial y_j} &= \frac{P}{4} \frac{\partial}{\partial y_j} \sum_{k=1}^{N} \begin{pmatrix} y_{b(k)} - y_{b(k+1)} \\ x_{b(k+1)} - x_{b(k)} \end{pmatrix} \cdot \begin{pmatrix} x_{b(k)} + x_{b(k+1)} \\ y_{b(k)} + y_{b(k+1)} \end{pmatrix} \\
&= \frac{P}{4} \frac{\partial}{\partial y_j} \sum_{k=1}^{N} (x_{b(k)} + x_{b(k+1)})(y_{b(k)} - y_{b(k+1)}) + (x_{b(k+1)} - x_{b(k)})(y_{b(k)} + y_{b(k+1)}), \\
&= \frac{P}{4} \sum_{k=1}^{N} (x_{b(k)} + x_{b(k+1)})(\delta_{j,b(k)} - \delta_{j,b(k+1)}) + (x_{b(k+1)} - x_{b(k)})(\delta_{j,b(k)} + \delta_{j,b(k+1)}), \\
&= \frac{P}{4} \left[(x_j + x_{j+}) - (x_{j-} + x_j) + (x_{j+} - x_j) + (x_j - x_{j-}) \right], \\
&= \frac{P}{2} \left(x_{j+} - x_{j-} \right),
\end{aligned}
$$

where $j+$ $(j-)$ is the node ahead of (behind) node j, as the boundary nodes are traversed anti-clockwise. In summary,

$$
\boxed{\nabla_{\mathbf{x}} \Pi_4 = -\frac{P\mathbf{Dy}}{2}, \qquad \nabla_{\mathbf{y}} \Pi_4 = \frac{P\mathbf{Dx}}{2},}
$$

and the matrix $\mathbf{D}$ is defined by

$$
D_{ij} = \begin{cases} +1, & \text{if nodes } i \text{ and } j \text{ are on the inner boundary and } j \text{ is 'ahead' of } i, \\ -1, & \text{if nodes } i \text{ and } j \text{ are on the inner boundary and } j \text{ is 'behind' } i, \\ 0, & \text{if one or both of nodes } i, j \text{ do not lie on the inner boundary.} \end{cases} \tag{89}
$$

Note that $\mathbf{D}$ is skew-symmetric: $\mathbf{D}^T = -\mathbf{D}$.

4.3 Minimum norm solution via QR factorization

In general the position field that makes (53) stationary is not unique. By construction, rigid body translations and rotations of any given solution will also make the functional (53) stationary and the Jacobian matrix $\mathbf{J}$ in (62) at any of these solutions will have a nullspace with dimension greater than zero. To select a single solution, we aim to find $\delta \mathbf{z}$ at each step of the Newton iteration that has minimum norm via the QR factorization of $\mathbf{J}^T$. The strain energy (53) may also admit multiple solutions that are *not* related by rigid body transformations. In theory, these different solutions could be found by seeding the Newton iteration with different initial guesses.

To resolve the multiplicity from rigid body transformations, first we decompose the square matrix $\mathbf{J}^T$ as

$$
\mathbf{J}^T \mathbf{P} = \mathbf{QR}, \tag{90}
$$

for an orthogonal square matrix $\mathbf{Q}$, an upper triangular $\mathbf{R}$ (unrelated to the $\mathbf{R}$ in eqs. (56),(57)) and a permutation matrix $\mathbf{P}$ which is chosen so that the diagonal entries of $\mathbf{R}$ are

in decreasing order of magnitude. Then, introducing $\delta\mathbf{w} \equiv \mathbf{Q}^T\delta\mathbf{z}$,

$$
\begin{aligned}
\mathbf{J}\delta\mathbf{z} &= -\mathbf{f}, \\
\Rightarrow \mathbf{R}^T\mathbf{Q}^T\delta\mathbf{z} &= -\mathbf{P}^T\mathbf{f}, \\
\Rightarrow \mathbf{R}^T\delta\mathbf{w} &= -\mathbf{P}^T\mathbf{f}.
\end{aligned}
\tag{91}
$$

If $\mathbf{R}^T$ is non-singular, then all of its diagonal entries are non-zero. But generally, $\mathbf{J}$ – and therefore $\mathbf{J}^T\mathbf{P}$ – will be singular and will have a nullspace of dimension $k > 0$. As a result, the final k diagonal entries of $\mathbf{R}$ will be zero and the solution to (91) will either not exist or be non-unique. We disregard the first case by assuming $-\mathbf{P}^T\mathbf{f} \in \text{Range}(\mathbf{R}^T)$. Then the non-uniqueness can be resolved in the following way.

Writing $\delta\mathbf{w} = \begin{pmatrix} \delta\mathbf{w}_1 \\ \delta\mathbf{w}_2 \end{pmatrix}$ where $\delta\mathbf{w}_1 \in \mathbb{R}^{2n-k}$ and $\delta\mathbf{w}_2 \in \mathbb{R}^k$, we can rewrite eq. (91) as

$$
\begin{bmatrix} \mathbf{R}_1^T & \mathbf{R}_2^T \end{bmatrix} \begin{pmatrix} \delta\mathbf{w}_1 \\ \delta\mathbf{w}_2 \end{pmatrix} = \mathbf{R}_1^T\delta\mathbf{w}_1 + \mathbf{R}_2^T\delta\mathbf{w}_2 = -\mathbf{P}^T\mathbf{f},
\tag{92}
$$

where $\mathbf{R}_1^T \in \mathbb{R}^{2n\times(2n-k)}$ is the full-rank submatrix consisting of the first $2n - k$ columns of $\mathbf{R}^T$, $\mathbf{R}_2^T$ is the submatrix consisting of the final k columns and $\text{Range}(\mathbf{R}_1^T) = \text{Range}(\mathbf{R}^T)$. When $\delta\mathbf{w}_2$ is chosen such that $\mathbf{R}_2^T\delta\mathbf{w}_2 = \mathbf{0}$, the resulting system is overdetermined and a unique solution for $\delta\mathbf{w}_1$ can be found in terms of the pseudo-inverse:

$$
\delta\mathbf{w}_1 = -\left(\mathbf{R}_1^T\right)^\dagger \mathbf{P}^T\mathbf{f},
\tag{93}
$$

where $\left(\mathbf{R}_1^T\right)^\dagger$ is the pseudo-inverse of $\mathbf{R}_1^T$. Then the general solution to (91) is

$$
\delta\mathbf{w} = \begin{pmatrix} -\left(\mathbf{R}_1^T\right)^\dagger \mathbf{P}^T\mathbf{f} \\ \delta\mathbf{w}_2 \end{pmatrix}.
\tag{94}
$$

Clearly, $\delta\mathbf{w}$ has minimum norm when $\delta\mathbf{w}_2 \equiv \mathbf{0}$:

$$
\delta\mathbf{w}_{\min} = \begin{pmatrix} -\left(\mathbf{R}_1^T\right)^\dagger \mathbf{P}^T\mathbf{f} \\ \mathbf{0} \end{pmatrix} \Rightarrow \delta\mathbf{z}_{\min} = \mathbf{Q}\begin{pmatrix} -\left(\mathbf{R}_1^T\right)^\dagger \mathbf{P}^T\mathbf{f} \\ \mathbf{0} \end{pmatrix},
\tag{95}
$$

Note that since $\delta\mathbf{z} = \mathbf{Q}\delta\mathbf{w}$, $||\delta\mathbf{z}|| = ||\delta\mathbf{w}||$ and finding the $\delta\mathbf{w}$ with minimum norm gives $\delta\mathbf{z}$ with minimum norm.

4.4 Stress Computation

In compressible morphoelasticity, the Cauchy stress is given by

$$
\boldsymbol{\sigma} = \frac{2}{J_e}\mathbf{F}_e\frac{\partial W}{\partial \mathbf{C}_e}\mathbf{F}_e^T,
\tag{96}
$$

where $W = W_k$ for $k = 1$ (intima), $k = 2$ (media) and $k = 3$ (adventitia) is given in eq. (30). With the relations

$$
\frac{\partial I_1}{\partial \mathbf{C}_e} = \mathbf{I}, \qquad \frac{\partial I_4}{\partial \mathbf{C}_e} = \mathbf{b} \otimes \mathbf{b}, \qquad \frac{\partial J_e}{\partial \mathbf{C}_e} = \frac{J_e}{2}\mathbf{F}_e^{-1}\mathbf{F}_e^{-T},
\tag{97}
$$

24

we have

$$\frac{\partial W}{\partial \mathbf{C}_e} = \frac{\mu \mathbf{I}}{2} + 2\eta \mathbf{H}_2 e^{H_1} + \frac{\nu\mu(J_e - 1)J_e}{1 - 2\nu}\mathbf{F}_e^{-1}\mathbf{F}_e^{-T} - \frac{\mu}{2}\mathbf{F}_e^{-1}\mathbf{F}_e^{-T}, \tag{98}$$

where

$$\begin{align}
H_1 &= \beta\left[\rho(I_4 - 1)_+^2 + (1 - \rho)(I_1 - 3)^2\right], \tag{99}\\
\mathbf{H}_2 &= \rho(I_4 - 1)_+(\mathbf{b} \otimes \mathbf{b}) + (1 - \rho)(I_1 - 3)\mathbf{I}. \tag{100}
\end{align}$$

Therefore the Cartesian Cauchy stress tensor is

$$\boldsymbol{\sigma} = \frac{2}{J_e}\left[\frac{\mu}{2}(\mathbf{F}_e\mathbf{F}_e^T - \mathbf{I}) + 2\eta e^{H_1}\mathbf{F}_e\mathbf{H}_2\mathbf{F}_e^T + \frac{\nu\mu(J_e - 1)J_e\mathbf{I}}{1 - 2\nu}\right]. \tag{101}$$

We can also consider stresses along and orthogonal to the projection of the fibers in the $x - y$ plane. The transformed stress tensor is

$$\boldsymbol{\sigma}^{(\text{fib})} = \mathbf{R}_c^T \boldsymbol{\sigma} \mathbf{R}_c \tag{102}$$

where

$$\mathbf{R}_c = \begin{pmatrix} \frac{c_1}{\sqrt{c_1^2 + c_2^2}} & -\frac{c_2}{\sqrt{c_1^2 + c_2^2}} & 0 \\ \frac{c_2}{\sqrt{c_1^2 + c_2^2}} & \frac{c_1}{\sqrt{c_1^2 + c_2^2}} & 0 \\ 0 & 0 & 1 \end{pmatrix} \tag{103}$$

and $\mathbf{c} = (c_1, c_2, c_3)^T = \mathbf{F}_e\mathbf{b}$ is the deformed fiber field at position (X, Y). In the special case where Ω_k, $k = 1, 2, 3$ are concentric annuli, $\sigma_{11}^{(\text{fib})}$ is the hoop/circumferential stress while $\sigma_{22}^{(\text{fib})}$ is the radial stress.

5   Results and Discussion

Before applying the code to pseudo-realistic arterial cross sections, we compare our results with an axisymmetric model that is based on solving the strong form boundary value problem (see Appendix A.2). In this 1D model each layer is neo-Hookean and all relevant quantities only depend on radial position. Figure 4 shows a pointwise comparison of the position field, Cauchy radial stress and Cauchy hoop stress. The fields are presented using the radial position of the reference frame R as the independent variable. Rather than taking a radial cut of the 2D finite element solution to make the comparison, the Cartesian coordinates of every node in the reference frame mesh are converted to a radial position and represented in Figure 4. There is good agreemeent in the deformed radial position $r(R)$, although the finite element solution will 'scatter' around the 1D model solution as ν approaches 0.5, the incompressible limit. This 'scatter' is much more evident in the stress fields since errors amplify when the fields are differentiated. In (b) and (c), stresses are computed on element faces and are not projected onto mesh points. We see that even when $\nu = 0.1$ there are deviations in the stress fields from the 1D model due to element locking. Nevertheless since the position fields are in good agreement, and the scatter in the stress is not systematic, we
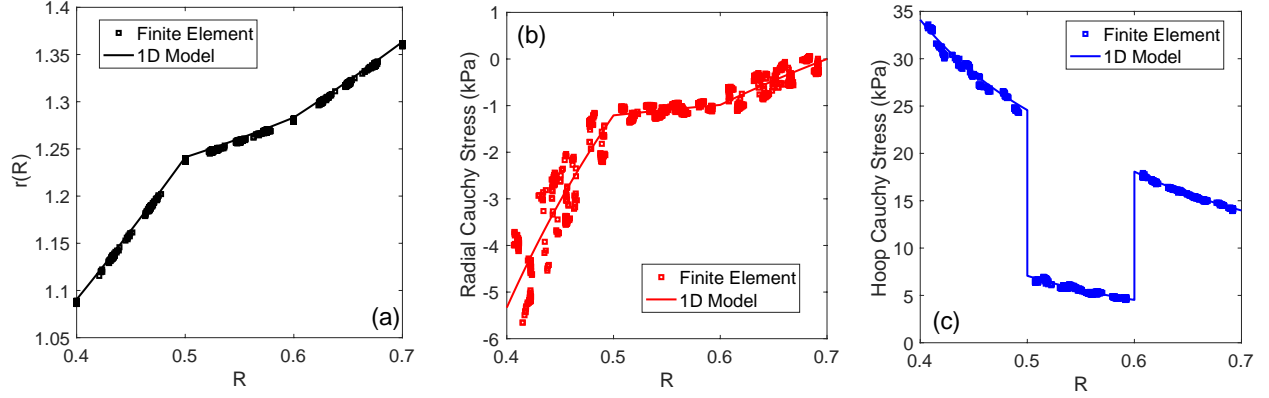
Figure 4: Radial position field, radial stress and circumferential (hoop) stress in finite element method versus 1D neo-Hookean model. Growth only occurs in the intima. Parameters: $(A, B, C, D) = (0.4, 0.5, 0.6, 0.7)$, $g_0 = 1.732$, $\nu = 0.1$. Material parameters are as in Table 1 but with $\eta_1 = \eta_2 = \eta_3 = 0$ and $P = 40$ mmHg. Mesh contained about 2400 elements.
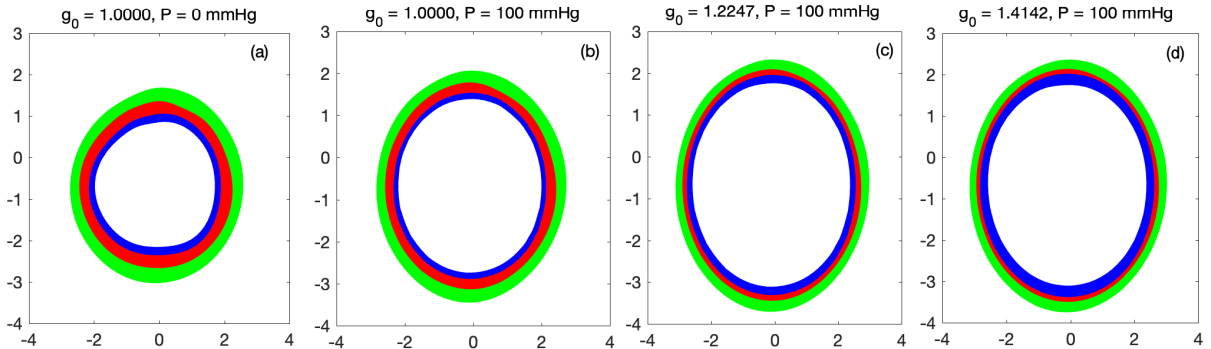
Figure 5: Pressurized growth of intima in a multi-layer arterial cross-section. Intima is shown in blue, media in red and adventitia in green. (a) Reference configuration. (b) Pressurized configuration. (c,d) Grown and pressurized configurations. Poisson ratio $\nu = 0.3$ and mechanical parameters are shown in Table 1. Finite element mesh consisted of about 2600 elements. Pressure P was increased to 100 mmHg using 11 uniform steps. Discretization of g_0 followed $g_0^{(i)} = \sqrt{1 + t_i}$ where $t_i = (i - 1)/60$, $i = 1, \ldots, 61$.
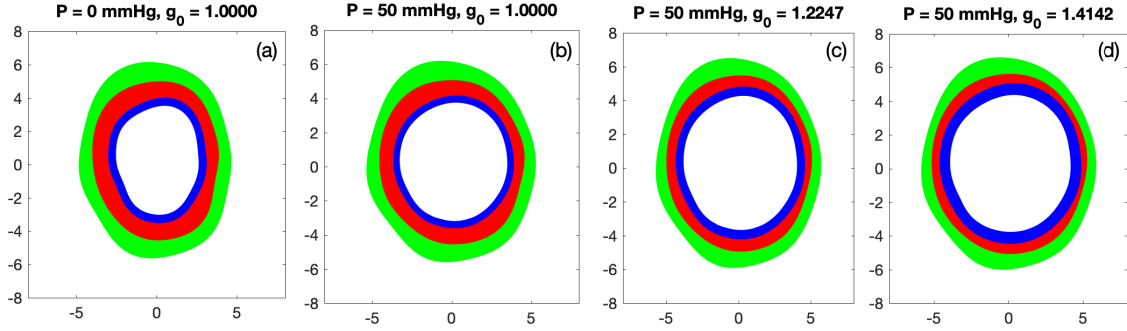
Figure 6: Growth of intima in a multi-layer arterial cross-section with Poisson ratio $\nu = 0.3$. Pressure was increased to $P = 50$ mmHg using 6 uniform steps. The finite element mesh consisted of about 3300 elements. Discretization of g_0 followed $g_0^{(i)} = \sqrt{1 + t_i}$ where $t_i = (i-1)/120$, $i = 1, \ldots, 121$.

can be fairly confident that our morphoelastic finite element method is consistent with the strong form boundary value problem (23)-(27) with $P_1 = P$ and $P_2 = 0$. In particular, note that the radial stress is continuous but the hoop stress presents discontinuities across the intima/media and media/adventitia interfaces.

In Figure 5, we show a simulated buildup of neo-intima as g_0 increases for a pressurized artery. Figure 5(a) shows the reference configuration corresponding to $(g_0 = 1, P = 0 \text{ mmHg})$, which is taken from a rat's carotid artery, while figures (b-d) show grown/deformed cross sections: elements in the intima (highlighted in blue) are g_0^2 times larger than in (a). Because of the lumen pressure, the cross sections in (b-d) are approximately circular. The geometry in (a) is represented by four polar curves $r = f_k(\theta)$, $k = 1, 2, 3, 4$ and each periodic f_k is in turn represented by the first seven terms of a Fourier series. Figure 6 is similar to Figure 5 but is taken from the cross section of a swine's coronary artery and we use a smaller lumen pressure $P = 50$ mmHg.

We now investigate the stability of the lumen-intima interface with respect to an increase in g_0. In Figure 7 we study how an imposed initial oscillation to the lumen-intima interface of the form $0.03 \cos 3\theta$ (where θ is the angle from the X axis) grows with g_0 when $P = 0$. We find that this long-wave oscillation (long compared to a typical element diameter) is unstable: the amplitude of the wave clearly increases as g_0 increases. An important consequence of this finding is that an axisymmetric artery that undergoes growth in the intima eventually develops instabilities that break symmetry. The addition of a lumen pressure may delay, but not prevent, the onset of these instabilities.

We have already seen in Fig. 4 that locking causes a 'scattering' of the numerical solution about the true solution. We now discuss this instability and a way to smooth out the scattered field. For each layer in the artery, the Cauchy stress is computed using eq. (96) with $\mathbf{F}_e$, $\mathbf{C}_e$ and J_e all numerically computed on faces, rather than nodes. Therefore the stress $\boldsymbol{\sigma}$ is a tensor that changes from element to element. To convert this into a nodal solution, we "project" by computing the nodal stress as a (non-weighted) average of stresses from
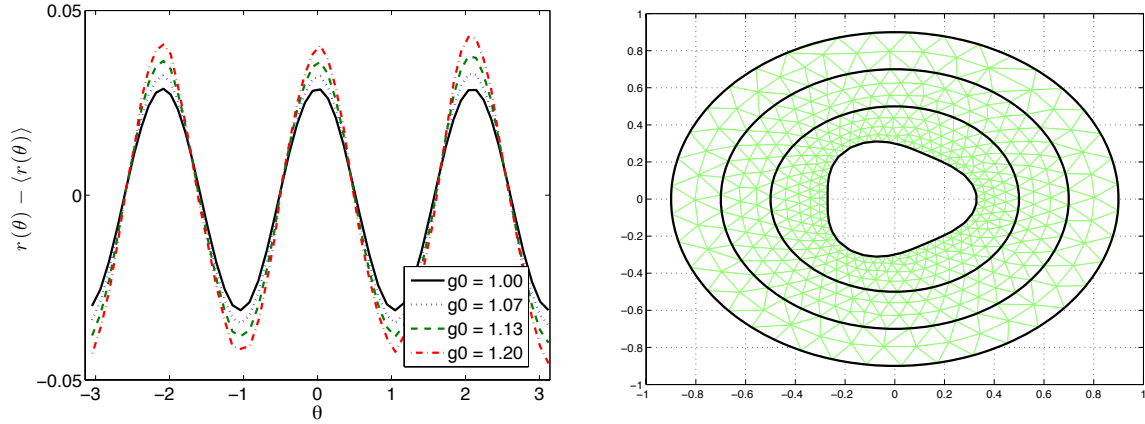
Figure 7: Left: Instability of an imposed periodic oscillation in the lumen-intima interface. Right: mesh used for the study. The inner boundary has the form $r(\theta) = 0.3 + 0.03\cos(3\theta)$. The radii of the remaining circular interfaces are 0.5, 0.7 and 0.9. Growth occurs without any lumen pressure.
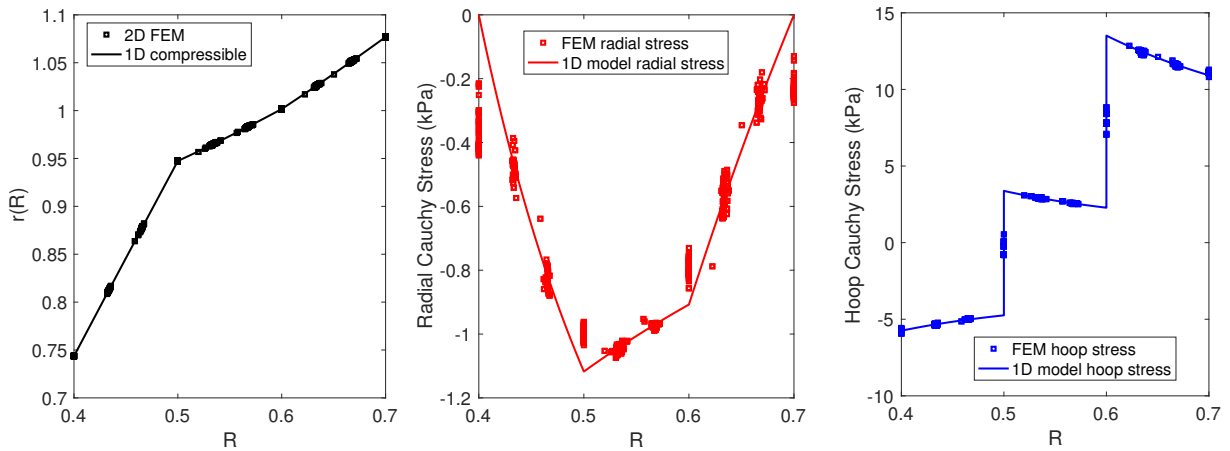
Figure 8: Comparison of radial position field, radial stress and circumferential (hoop) stress between finite element method and 1D neo-Hookean model. Growth only occured in the intima. Parameters: $(A, B, C, D) = (0.4, 0.5, 0.6, 0.7)$, $g_0 = 2$ in the intima, $\nu = 0.3$. Material parameters are as in Table 1 but with $\eta_1 = \eta_2 = \eta_3 = 0$ and $P = 0$ mmHg. Mesh contained about 1700 elements. Stress fields at nodes were computed by taking the average of adjacent faces. Note large discrepencies in the finite element radial stress at $R = 0.4$ and $R = 0.7$ stemming from the smoothing procedure.

28
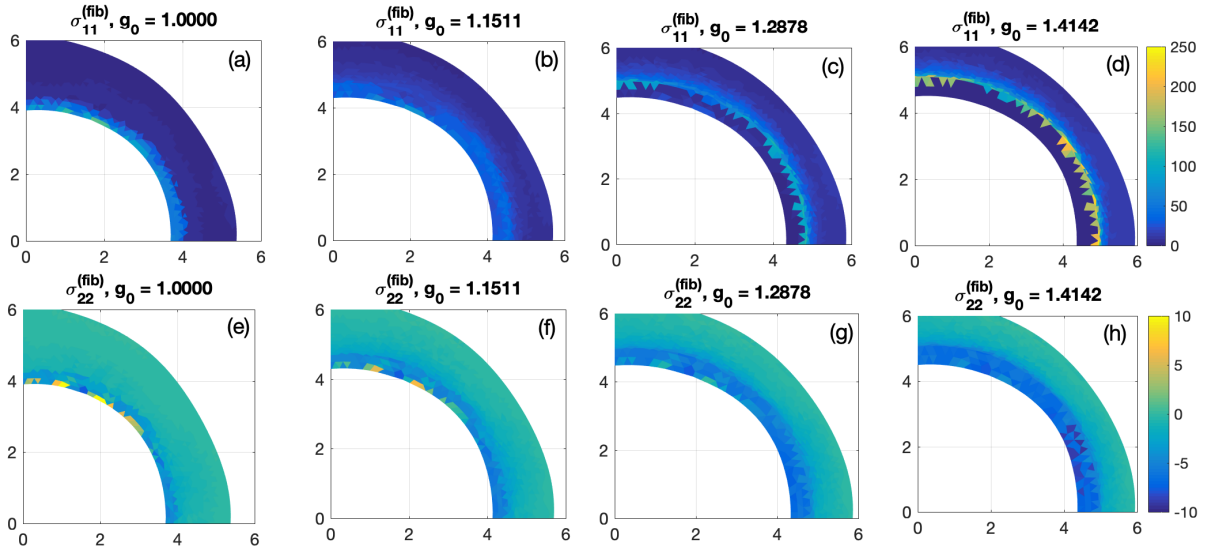
Figure 9: Tractions along ($\sigma_{11}^{(\text{fib})}$, upper row) and perpendicular to ($\sigma_{22}^{(\text{fib})}$, lower row) wall fibers as a function of growth g_0 with $P = 50$ mmHg. Mechanical parameters are shown in Table 1. Poisson ratio $\nu = 0.3$ and mesh consisted of about 5700 elements. Units of color axis are in kPa. Pressure was increased to $P = 50$ mmHg using 6 uniform steps. Discretization of g_0 followed $g_0^{(i)} = \sqrt{1 + t_i}$ where $t_i = (i - 1)/120$, $i = 1, \ldots, 121$.
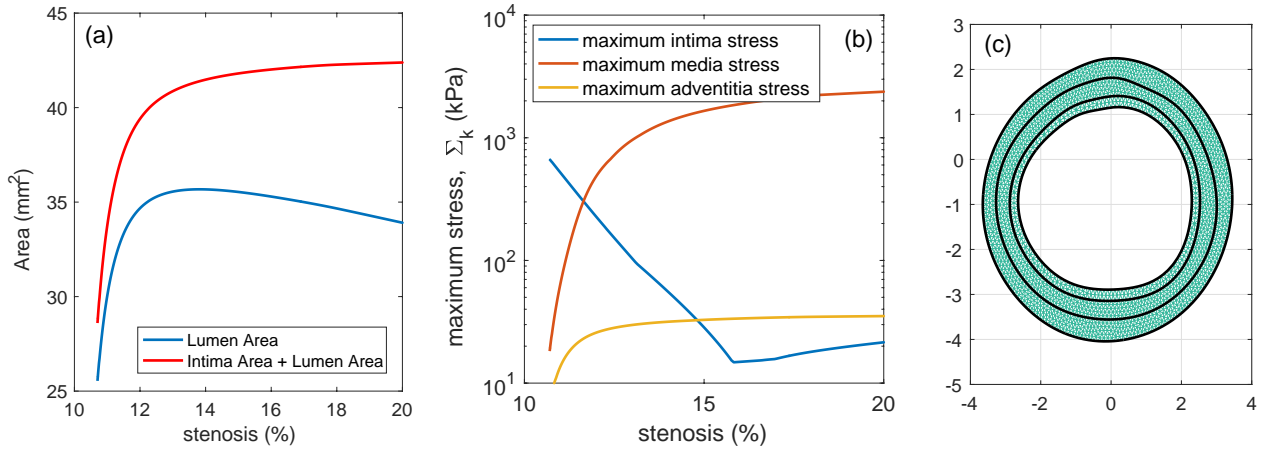
Figure 10: Remodeling behavior of multi-layer arterial cross-section. Left: Lumen area increases and then decreases as a function of stenosis, consistent with Glagov remodeling. The area enclosed by the internal elastic lamina (i.e. sum of intima and lumen areas) abruptly stops increasing after a critical stenosis of about 13%. Center: Maximum Cauchy stress Σ_k, $k = 1, 2, 3$ (defined in eq. (104)) for each arterial layer as a function of stenosis. The media eventually bears the maximum stress. Lumen pressure was $P = 100$ mmHg, Poisson ratio $\nu = 0.3$. Right: Mesh used for the simulation, consisting of about 3800 elements.

elements that share that node. This has the effect of smoothing out the solution. However, when ν is close to 0.5, the elemental solution still suffers from large oscillations that stem from $(J_e - 1)$ in eq. (101) alternating its sign on adjacent elements. This "checkerboard" phenomenon is especially prominent for annular domains with highly uniform (triangular) elements. The smoothed nodal solution gives a reasonable approximation of the exact stress providing the number of elements that share the node is even, which is generally the case for internal nodes. However, boundary nodes are almost always shared by 3 adjacent elements with the result that stresses on the boundary can exhibit very poor accuracy under this averaging method: see Fig. 8.

With these limitations of the stress computation in mind, we investigate the stresses that develop as the arterial section undergoes growth. In Fig. 9 we show the smoothed stress tensor fields $\sigma_{11}^{(\text{fib})}$ and $\sigma_{22}^{(\text{fib})}$ as g_0 increases. Although the geometry is not axisymmetric, we will refer to these as circumferential and radial stresses respectively (more precisely, they are tractions tangential to and orthogonal to the local fiber vector). The circumferential stress $\sigma_{11}^{(\text{fib})}$ is about an order of magnitude greater than the radial stress $\sigma_{22}^{(\text{fib})}$. The maximum circumferential stress occurs adjacent to the lumen (i.e. near the interface between the lumen and the intima) when $g_0 = 1$. However, when g_0 increases we see that the maximum stress migrates outwards and eventually the interface between the intima and media bears the most stress. This is also consistent with intuition since only the intima is growing but material elements in this layer are perfectly bonded to adjacent elements in the media.

We can also use our method to monitor how the maximum stress increases within each layer. In Fig. 10, we investigate how the quantity

$$\Sigma_k = \max_{(x,y)\in\text{layer }k} \left\{ ||\sigma_{11}^{(\text{fib})}||_\infty, ||\sigma_{12}^{(\text{fib})}||_\infty, ||\sigma_{21}^{(\text{fib})}||_\infty, ||\sigma_{22}^{(\text{fib})}||_\infty \right\}, \qquad (104)$$

for $k = 1$ (intima), 2 (media), and 3 (adventitia) evolves as the intima thickens. We quantify the progression of disease through the stenosis percentage, defined as $100\times$ (intima area)/(intima area + lumen area). The stenosis is close to zero for a healthy artery with very little intima, is equal to one hundred for an artery whose lumen is completely occluded, and increases as g_0 increases. In Fig. 10(a) we see that the lumen area is non-monotonic with respect to stenosis: there is a phase where the lumen area rapidly increases and a separate phase where it decreases. The switch in behavior occurs at a critical stenosis of about 13%. The presence of two separate "phases" in the remodeling curve is reminiscent of Glagov phenomenon [28] which predicts a mild initial increase in the lumen area (with respect to stenosis) followed by a rapid encroachment phase. In our results, the second phase corresponds to a gradual occlusion of the lumen while the area enclosed by the internal elastic lamina (red) remains approximately constant. In Fig. 10(b) we show how the stresses change with growth. The most striking feature is that the maximum intima stress decreases until the stenosis reaches about 16%, after which it gradually increases. The media bears more and more of the stress as stenosis increases while the stress on the adventitia is much smaller and fairly insensitive to stenosis. For reference, it is worth bearing in mind that the rupture stress for atherosclerotic plaques is estimated at between 300 and 500 kPa [29, 30] and our simulations suggest this level of stress could be easily reached for stenoses exceeding 10%. This appears unrealistic since many unruptured lesions with stenosis much larger than 10%

have been observed. However, the stress magnitudes generated by our simulations are very sensitive to the thickness of individual layers in the reference configuration and should not be taken literally. Rather, the key qualitative result here is that stresses can be modeled as dynamic quantities that exhibit non-monotonic behavior, and such behavior may be related to the switch from compensatory to inward remodeling.

6   Summary and Conclusions

In this paper we presented a 2D finite element method for simulating intimal thickening of arterial cross sections using compressible morphoelasticity theory. The foundation of our method is the energy functional (53). Recall that in morphoelasticity theory, elements first undergo stress-free growth and then an elastic deformation. The growth step does not change the energy of the area element dA. However, the elastic deformation does and the area integrand $W(\mathbf{F}_e)J_g \cdot dA$ represents the change in energy associated with elastically deforming *grown* elements, where J_g is the growth Jacobian, $\mathbf{F}_e$ is the elastic deformation gradient and W is the strain energy density. In contrast, since only the elastic part of the deformation can induce a stress, the Cauchy stress is completely independent of growth and depends only on $\mathbf{F}_e$ (see eq. (96)). In our numerical experiments, we found that using $\int_\Omega W(\mathbf{F}_e)dA$ instead of $\int_\Omega W(\mathbf{F}_e)J_g dA$ in the volumetric energy results in a discontinuous normal stress across interfaces.

In terms of the numerical method, the main novelty is that we treat the artery wall as three separate layers, each with its own unique mechanical properties. Each layer is modeled as a hyperelastic, fiber-reinforced composite and only the intima is allowed to grow. By organizing our variables into two groups, the x-position fields and y-position fields, our resulting system of nonlinear algebraic equations can be broken up into blocks and the Jacobian matrix derived in terms of these blocks. An explicit expression for the Jacobian allows the use of the Newton-Raphson method for rapid convergence of the position fields. Non-uniqueness of the deformed state (with respect to rigid body transformation) is handled by using a QR decomposition to select the solution with minimum norm.

Our results suggest that as the intima grows, the maximum Cauchy stress eventually concentrates along intima-media boundaries and increases with growth. It is possible that the large stress at these locations could promote delamination or a local tissue atrophy. The results also predict that the media is the layer in the vessel wall that bears the largest stress. In contrast, static studies of arteries suggest that the adventitia bears the most stress [3]. However, one must be careful when comparing with these different studies because in our model we assume that the unloaded healthy artery (with $P = 0$ and $g_0 = 1$) is not residually stressed. Also, our simulation results correspond to the specific parameter values listed in Table 1. We have not explored how the stress fields change when different parameter values are used, or when the layers are described by other kinds of strain energy. When stresses are regarded as dynamic with respect to growth, their evolution shows a rich behavior. Maximum stresses can be non-monotonic and our studies show that inflection points may be linked to Glagov remodeling.

There are several issues that still need to be resolved. The biggest weakness of our method

is that it is prone to locking. Locking manifests itself as a checkerboard instability in the stress field (and to a lesser extent, the position field). This kind of behavior can be avoided through multi-field approaches such as the Hu-Washizu method [31, 32], so generalizing these types of approaches to the morphoelastic setting is an important extension. Another important issue, specific to arterial modeling, is the separation of length scales in vessel wall structure. Healthy intima is very thin (tens of micrometers), while the media and adventitia are relatively thick (millimeters). In the current framework, we allow the reference intima thickness to be half or a quarter of the media thickness and then mesh every layer with elements of the same size. This is obviously not ideal but attempts to allow the mesh width to gradually increase in the media and adventitia almost always resulted in non-convergence of the Newton method. Simulating the arterial wall is inherently a multi-scale problem and we believe that developing fast and efficient multi-scale methods for morphoelasticity problems will be important challenges for the future.

References

[1] A. Goriely and M. B. Amar. On the definition and modeling of incremental, cumulative, and continuous growth laws in morphoelasticity. *Biomechanics and Modeling in Mechanobiology*, 6(5):289–296, 2007.

[2] E. K. Rodriguez, A. Hoger, and A. D. McCulloch. Stress-dependent finite growth in soft elastic tissues. *Journal of Biomechanics*, 27(4):455–467, 1994.

[3] G. A. Holzapfel, G. Sommer, C. T. Gasser, and P. Regitnig. Determination of layer-specific mechanical properties of human coronary arteries with nonatherosclerotic intimal thickening and related constitutive modeling. *American Journal of Physiology-Heart and Circulatory Physiology*, 289(5):H2048–H2058, 2005.

[4] P. Badel, S. Avril, S. Lessner, and M. Sutton. Mechanical identification of hyperelastic anisotropic properties of mouse carotid arteries. In *Mechanics of Biological Systems and Materials, Volume 2*, pages 11–17. Springer, 2011.

[5] T. C. Gasser, R. W. Ogden, and G. A. Holzapfel. Hyperelastic modelling of arterial layers with distributed collagen fibre orientations. *Journal of the Royal Society Interface*, 3(6):15–35, 2006.

[6] M. L. Stadius, A. M. Gown, R. Kernoff, and C. L. Collins. Cell proliferation after balloon injury of iliac arteries in the cholesterol-fed New Zealand white rabbit. *Arteriosclerosis, Thrombosis, and Vascular Biology*, 14(5):727–733, 1994.

[7] A. Jawien, D. F. Bowen-Pope, V. Lindner, S. M. Schwartz, and A. W. Clowes. Platelet-derived growth factor promotes smooth muscle migration and intimal thickening in a rat model of balloon angioplasty. *The Journal of Clinical Investigation*, 89(2):507–511, 1992.

[8] Y. Nakashima, T. N. Wight, and K. Sueishi. Early atherosclerosis in humans: role of diffuse intimal thickening and extracellular matrix proteoglycans. *Cardiovascular Research*, 79(1):14–23, 2008.

[9] S. M. Schwartz, D. deBlois, and E. R. M. O'Brien. The intima: soil for atherosclerosis and restenosis. *Circulation Research*, 77(3):445–465, 1995.

[10] K. Gou and T. J Pence. Computational modeling of tracheal angioedema due to swelling of the submucous tissue layer. *International Journal for Numerical Methods in Biomedical Engineering*, 33(10), 2017.

[11] D. Ambrosi, G. A. Ateshian, E. M. Arruda, S. C. Cowin, J. Dumais, A. Goriely, G. A. Holzapfel, J. D. Humphrey, R. Kemkemer, E. Kuhl, J. E. Olberding, Taber L. A., and K. Garikipati. Perspectives on biological growth and remodeling. *Journal of the Mechanics and Physics of Solids*, 59(4):863–883, 2011.

[12] H. Byrne and L. Preziosi. Modelling solid tumour growth using the theory of mixtures. *Mathematical Medicine and Biology: a journal of the IMA*, 20(4):341–366, 2003.

[13] A. B. Tepole, C. J. Ploch, J. Wong, A. K. Gosain, and E. Kuhl. Growing skin: a computational model for skin expansion in reconstructive surgery. *Journal of the Mechanics and Physics of Solids*, 59(10):2177–2190, 2011.

[14] E. Kuhl, R. Maas, G. Himpel, and A. Menzel. Computational modeling of arterial wall growth. *Biomechanics and Modeling in Mechanobiology*, 6(5):321–331, 2007.

[15] P. W. Alford and L. A. Taber. Computational study of growth and remodelling in the aortic arch. *Computer Methods in Biomechanics and Biomedical Engineering*, 11(5):525–538, 2008.

[16] Javier Rodríguez, Jose M Goicolea, and Felipe Gabaldon. A volumetric model for growth of arterial walls with arbitrary geometry and loads. *Journal of biomechanics*, 40(5):961–971, 2007.

[17] S. Budday, C. Raybaud, and E. Kuhl. A mechanical model predicts morphological abnormalities in the developing human brain. *Scientific Reports*, 4:5644, 2014.

[18] P. Podio-Guidugli. A variational approach to live loadings in finite elasticity. *Journal of elasticity*, 19(1):25–36, 1988.

[19] J. M Ball. Convexity conditions and existence theorems in nonlinear elasticity. *Archive for rational mechanics and Analysis*, 63(4):337–403, 1976.

[20] P. G. Ciarlet. *Mathematical elasticity Vol. 1: Threedimensional elasticity.* Amsterdam, 1987.

[21] Martine Ben Amar and Alain Goriely. Growth and instability in elastic tissues. *Journal of the Mechanics and Physics of Solids*, 53(10):2284–2319, 2005.

[22] Si-Fan Yin, Shi-Lei Xue, Bo Li, and Xi-Qiao Feng. Bio–chemo–mechanical modeling of growing biological tissues: Finite element method. *International Journal of Non-Linear Mechanics*, 108:46–54, 2019.

[23] T. J. Pence and K. Gou. On compressible versions of the incompressible neo-Hookean material. *Mathematics and Mechanics of Solids*, 20(2):157–182, 2015.

[24] G. A. Holzapfel. Biomechanics of soft tissue. *The Handbook of Material Behavior*, 2000.

[25] Daniel Balzani, Patrizio Neff, Jörg Schröder, and Gerhard A Holzapfel. A polyconvex framework for soft biological tissues. adjustment to experimental data. *International journal of solids and structures*, 43(20):6052–6070, 2006.

[26] P.-W. Fok. Multi-layer mechanical model of glagov remodeling in coronary arteries: Differences between in-vivo and ex-vivo measurements. *PLoS One*, 11(7):e0159304, 2016.

[27] P.-O. Persson and G. Strang. A simple mesh generator in matlab. *SIAM Review*, 46(2):329–345, 2004.

[28] S. Glagov, E. Weisenberg, C. K. Zarins, R. Stankunavicius, and G. J. Kolettis. Compensatory enlargement of human atherosclerotic coronary arteries. *New England Journal of Medicine*, 316(22):1371–1375, 1987.

[29] A. Kelly-Arnold, N. Maldonado, D. Laudier, E. Aikawa, L. Cardoso, and S. Weinbaum. Revised microcalcification hypothesis for fibrous cap rupture in human coronary arteries. *Proceedings of the National Academy of Sciences*, 110(26):10741–10746, 2013.

[30] G. C. Cheng, H. M. Loree, R. D. Kamm, M. C. Fishbein, and R. T. Lee. Distribution of circumferential stress in ruptured and stable atherosclerotic lesions. a structural analysis with histopathological correlation. *Circulation*, 87(4):1179–1187, 1993.

[31] Juan Carlos Simo. On a fully three-dimensional finite-strain viscoelastic damage model: formulation and computational aspects. *Computer methods in applied mechanics and engineering*, 60(2):153–173, 1987.

[32] Juan C Simo and Robert L Taylor. Quasi-incompressible finite elasticity in principal stretches. continuum basis and numerical algorithms. *Computer methods in applied mechanics and engineering*, 85(3):273–310, 1991.

[33] F. Clarke. On the inverse function theorem. *Pacific Journal of Mathematics*, 64(1):97–102, 1976.

[34] L. Qi and J. Sun. A nonsmooth version of Newton's method. *Mathematical Programming*, 58(1-3):353–367, 1993.

[35] M. J. Śmietański. Some quadrature-based versions of the generalized Newton method for solving nonsmooth equations. *Journal of Computational and Applied Mathematics*, 235(17):5131–5139, 2011.

A Appendix

A.1 Construction of K

The definition of the matrix $\mathbf{K}$ that appears in eq. (61) is

$$
\mathbf{K} = \begin{bmatrix} \dfrac{\partial \mathbf{\Gamma}}{\partial x_1}\mathbf{y} & \dfrac{\partial \mathbf{\Gamma}}{\partial x_2}\mathbf{y} & \cdots & \dfrac{\partial \mathbf{\Gamma}}{\partial x_n}\mathbf{y} & \dfrac{\partial \mathbf{\Gamma}}{\partial y_1}\mathbf{y} & \dfrac{\partial \mathbf{\Gamma}}{\partial y_2}\mathbf{y}\cdots & \dfrac{\partial \mathbf{\Gamma}}{\partial y_n}\mathbf{y} \\[2ex] -\dfrac{\partial \mathbf{\Gamma}}{\partial x_1}\mathbf{x} & -\dfrac{\partial \mathbf{\Gamma}}{\partial x_2}\mathbf{x} & \cdots & -\dfrac{\partial \mathbf{\Gamma}}{\partial x_n}\mathbf{x} & -\dfrac{\partial \mathbf{\Gamma}}{\partial y_1}\mathbf{x} & -\dfrac{\partial \mathbf{\Gamma}}{\partial y_2}\mathbf{x}\cdots & -\dfrac{\partial \mathbf{\Gamma}}{\partial y_n}\mathbf{x} \end{bmatrix} +
$$
$$(105)$$

$$
\begin{bmatrix} \dfrac{\partial \mathbf{R}}{\partial x_1}\mathbf{x} & \dfrac{\partial \mathbf{R}}{\partial x_2}\mathbf{x} & \cdots & \dfrac{\partial \mathbf{R}}{\partial x_n}\mathbf{x} & \dfrac{\partial \mathbf{R}}{\partial y_1}\mathbf{x} & \dfrac{\partial \mathbf{R}}{\partial y_2}\mathbf{x}\cdots & \dfrac{\partial \mathbf{R}}{\partial y_n}\mathbf{x} \\[2ex] \dfrac{\partial \mathbf{R}}{\partial x_1}\mathbf{y} & \dfrac{\partial \mathbf{R}}{\partial x_2}\mathbf{y} & \cdots & \dfrac{\partial \mathbf{R}_2}{\partial x_n}\mathbf{y} & \dfrac{\partial \mathbf{R}}{\partial y_1}\mathbf{y} & \dfrac{\partial \mathbf{R}}{\partial y_2}\mathbf{y}\cdots & \dfrac{\partial \mathbf{R}}{\partial y_n}\mathbf{y} \end{bmatrix} \in \mathbb{R}^{2n\times 2n},
$$

where $\mathbf{x} = (x_1,\ldots,x_n)^T$, $\mathbf{y} = (y_1,\ldots,y_n)^T$. For reference, let

$$
\tilde{\mathbf{\Gamma}} = \frac{2\nu}{1-2\nu}(\tilde{\mathbf{S}} - \tilde{\mathbf{E}}) - \tilde{\mathbf{V}} - \frac{P\tilde{\mathbf{D}}}{2}, \tag{106}
$$

$$
\Rightarrow \frac{\partial \tilde{\mathbf{\Gamma}}}{\partial z_{Q(k)}} = \frac{2\nu}{1-2\nu}\frac{\partial \tilde{\mathbf{S}}}{\partial z_{Q(k)}} - \frac{\partial \tilde{\mathbf{V}}}{\partial z_{Q(k)}}, \tag{107}
$$

where $z_{Q(k)} \in \{x_{Q(k)}, y_{Q(k)}\}$. To build the matrix $\mathbf{K}$, we first form an elemental counterpart corresponding to triangle Q:

$$
\widehat{\mathbf{K}} = \begin{bmatrix} \dfrac{\partial \tilde{\mathbf{\Gamma}}}{\partial x_{Q(1)}}\mathbf{y}_Q & \dfrac{\partial \tilde{\mathbf{\Gamma}}}{\partial x_{Q(2)}}\mathbf{y}_Q & \dfrac{\partial \tilde{\mathbf{\Gamma}}}{\partial x_{Q(3)}}\mathbf{y}_Q & \dfrac{\partial \tilde{\mathbf{\Gamma}}}{\partial y_{Q(1)}}\mathbf{y}_Q & \dfrac{\partial \tilde{\mathbf{\Gamma}}}{\partial y_{Q(2)}}\mathbf{y}_Q & \dfrac{\partial \tilde{\mathbf{\Gamma}}}{\partial y_{Q(3)}}\mathbf{y}_Q \\[2ex] -\dfrac{\partial \tilde{\mathbf{\Gamma}}}{\partial x_{Q(1)}}\mathbf{x}_Q & -\dfrac{\partial \tilde{\mathbf{\Gamma}}}{\partial x_{Q(2)}}\mathbf{x}_Q & -\dfrac{\partial \tilde{\mathbf{\Gamma}}}{\partial x_{Q(3)}}\mathbf{x}_Q & -\dfrac{\partial \tilde{\mathbf{\Gamma}}}{\partial y_{Q(1)}}\mathbf{x}_Q & -\dfrac{\partial \tilde{\mathbf{\Gamma}}}{\partial y_{Q(2)}}\mathbf{x}_Q & -\dfrac{\partial \tilde{\mathbf{\Gamma}}}{\partial y_{Q(3)}}\mathbf{x}_Q \end{bmatrix} +
$$

$$
\begin{bmatrix} \dfrac{\partial \tilde{\mathbf{R}}}{\partial x_{Q(1)}}\mathbf{x}_Q & \dfrac{\partial \tilde{\mathbf{R}}}{\partial x_{Q(2)}}\mathbf{x}_q & \dfrac{\partial \tilde{\mathbf{R}}}{\partial x_{Q(3)}}\mathbf{x}_Q & \dfrac{\partial \tilde{\mathbf{R}}}{\partial y_{Q(1)}}\mathbf{x}_Q & \dfrac{\partial \tilde{\mathbf{R}}}{\partial y_{Q(2)}}\mathbf{x}_Q & \dfrac{\partial \tilde{\mathbf{R}}}{\partial y_{Q(3)}}\mathbf{x}_Q \\[2ex] \dfrac{\partial \tilde{\mathbf{R}}}{\partial x_{Q(1)}}\mathbf{x}_Q & \dfrac{\partial \tilde{\mathbf{R}}}{\partial x_{Q(2)}}\mathbf{y}_Q & \dfrac{\partial \tilde{\mathbf{R}}}{\partial x_{Q(3)}}\mathbf{x}_Q & \dfrac{\partial \tilde{\mathbf{R}}}{\partial y_{Q(1)}}\mathbf{y}_Q & \dfrac{\partial \tilde{\mathbf{R}}}{\partial y_{Q(2)}}\mathbf{x}_Q & \dfrac{\partial \tilde{\mathbf{R}}}{\partial y_{Q(3)}}\mathbf{y}_Q \end{bmatrix} \in \mathbb{R}^{6\times 6},
$$

$$(108)$$

where $\mathbf{x}_q = (x_{Q(1)}, x_{Q(2)}, x_{Q(3)})^T$, $\mathbf{y}_Q = (y_{Q(1)}, y_{Q(2)}, y_{Q(3)})^T$ and $Q(1), Q(2), Q(3)$ are the vertices of element Q. Then we cycle through all n elements and update through $\mathbf{K} \leftarrow \mathbf{K} + \tilde{\mathbf{K}}$ where the matrix $\hat{\mathbf{K}} \in \mathbb{R}^{2n \times 2n}$ is defined by

$$\tilde{K}_{\varphi(i),\varphi(j)} = \widehat{K}_{ij}, \quad i = 1, 2, \ldots, 6, \quad j = 1, 2, \ldots, 6, \tag{109}$$

$$\varphi(i) = \begin{cases} Q(i), & i = 1, 2, 3, \\ Q(i-3) + n, & i = 4, 5, 6. \end{cases} \tag{110}$$

The matrices $\frac{\partial \tilde{\mathbf{S}}}{\partial x_{Q(k)}}$, $\frac{\partial \tilde{\mathbf{S}}}{\partial y_{Q(k)}}$, $\frac{\partial \tilde{\mathbf{V}}}{\partial x_{Q(k)}}$ and $\frac{\partial \tilde{\mathbf{V}}}{\partial y_{Q(k)}}$ from (107) are:

$$\frac{\partial \tilde{\mathbf{S}}}{\partial x_{Q(k)}} = \frac{\Delta_Q \mu_Q}{g_Q^2} \tilde{\mathbf{N}} \sum_{s=1}^{3} y_{Q(s)} \tilde{N}_{Q(k),Q(s)}, \tag{111}$$

$$\frac{\partial \tilde{\mathbf{S}}}{\partial y_{Q(k)}} = -\frac{\Delta_Q \mu_Q}{g_Q^2} \tilde{\mathbf{N}} \sum_{s=1}^{3} x_{Q(s)} \tilde{N}_{Q(k),Q(s)}, \tag{112}$$

$$\frac{\partial \tilde{\mathbf{V}}}{\partial x_{Q(k)}} = -\frac{\Delta_Q \mu_Q g_Q^2 \tilde{\mathbf{N}}}{\tilde{J}_Q^2} \sum_{s=1}^{s} y_{Q(s)} \tilde{N}_{Q(k),Q(s)}, \tag{113}$$

$$\frac{\partial \tilde{\mathbf{V}}}{\partial y_{Q(k)}} = +\frac{\Delta_Q \mu_Q g_Q^2 \tilde{\mathbf{N}}}{\tilde{J}_Q^2} \sum_{s=1}^{3} x_{Q(s)} \tilde{N}_{Q(k),Q(s)}, \tag{114}$$

$$\tilde{J}_Q = x_{Q(i)} y_{Q(j)} \tilde{N}_{Q(i),Q(j)}. \tag{115}$$

The elemental matrix $\tilde{\mathbf{R}}$ and its derivatives are computed as

$$\tilde{R}_{Q(i),Q(j)} = 4\Delta_Q \eta_Q e^{\beta_Q \rho_Q (\lambda_Q)_+^2 + \beta_Q(1-\rho_Q)\sigma_Q^2} \left\{ \rho_Q (\lambda_Q)_+ \tilde{L}_{Q(i),Q(j)} + (1 - \rho_Q)\sigma_Q \tilde{U}_{Q(i),Q(j)} \right\}.$$

The derivatives can be extracted from the matrices $\nabla_{\mathbf{x}_Q} \tilde{\mathbf{R}}, \nabla_{\mathbf{y}_Q} \tilde{\mathbf{R}} \in \mathbb{R}^{9 \times 3}$:

$$\left(\nabla_{\mathbf{x}_Q} \tilde{\mathbf{R}} \right)^T \overset{d}{=} \left[\begin{array}{ccc} \dfrac{\partial \tilde{\mathbf{R}}}{\partial x_{Q(1)}}, & \dfrac{\partial \tilde{\mathbf{R}}}{\partial x_{Q(2)}}, & \dfrac{\partial \tilde{\mathbf{R}}}{\partial x_{Q(3)}} \end{array} \right], \qquad \left(\nabla_{\mathbf{y}_Q} \tilde{\mathbf{R}} \right)^T \overset{d}{=} \left[\begin{array}{ccc} \dfrac{\partial \tilde{\mathbf{R}}}{\partial y_{Q(1)}}, & \dfrac{\partial \tilde{\mathbf{R}}}{\partial y_{Q(2)}}, & \dfrac{\partial \tilde{\mathbf{R}}}{\partial y_{Q(3)}} \end{array} \right],$$

(note that the transposition here operates on blocks) where

$$\nabla_{\mathbf{x}_Q} \tilde{\mathbf{R}} = 4\Delta_Q \eta_Q e^{\beta_Q \rho_Q (\lambda_Q)_+^2 + \beta_Q(1-\rho_Q)\sigma_Q^2} \times$$
$$\left(2\beta_Q \rho_Q (\lambda_Q)_+ \nabla_{\mathbf{x}_Q} (\lambda_Q)_+ + 2\beta_Q(1-\rho_Q)\sigma_Q \nabla_{\mathbf{x}_Q} \sigma_Q \right) \otimes \left(\rho_Q (\lambda_Q)_+ \tilde{\mathbf{L}} + (1-\rho_Q)\sigma_Q \tilde{\mathbf{U}} \right)$$
$$+ 4\Delta_Q \eta_Q e^{\beta_Q \rho_Q (\lambda_Q)_+^2 + \beta_Q(1-\rho_Q)\sigma_Q^2} \left(\rho_Q \nabla_{\mathbf{x}_Q} (\lambda_Q)_+ \otimes \tilde{\mathbf{L}} + (1-\rho_Q) \nabla_{\mathbf{x}_Q} \sigma_Q \otimes \tilde{\mathbf{U}} \right)$$

$$\nabla_{\mathbf{y}_Q} \tilde{\mathbf{R}} = 4\Delta_Q \eta_Q e^{\beta_Q \rho_Q (\lambda_Q)_+^2 + \beta_Q(1-\rho_Q)\sigma_Q^2} \times$$
$$\left(2\beta_Q \rho_Q (\lambda_Q)_+ \nabla_{\mathbf{y}_Q} (\lambda_Q)_+ + 2\beta_Q(1-\rho_Q)\sigma_Q \nabla_{\mathbf{y}_Q} \sigma_Q \right) \otimes \left(\rho_Q (\lambda_Q)_+ \tilde{\mathbf{L}} + (1-\rho_Q)\sigma_Q \tilde{\mathbf{U}} \right)$$
$$+ 4\Delta_Q \eta_Q e^{\beta_Q \rho_Q (\lambda_Q)_+^2 + \beta_Q(1-\rho_Q)\sigma_Q^2} \left(\rho_Q \nabla_{\mathbf{y}_Q} (\lambda_Q)_+ \otimes \tilde{\mathbf{L}} + (1-\rho_Q) \nabla_{\mathbf{y}_Q} \sigma_Q \otimes \tilde{\mathbf{U}} \right)$$

where λ_Q and σ_Q are given by eqs. (74) and (75) and

$$\nabla_{\mathbf{x}_Q}(\lambda_Q)_+ = g_Q^{-2}\left(\tilde{\mathbf{H}} + \tilde{\mathbf{H}}^T\right)\mathbf{x}_Q \cdot 1_{\lambda_Q > 0}(\mathbf{x}_Q, \mathbf{y}_Q), \tag{116}$$

$$\nabla_{\mathbf{y}_Q}(\lambda_Q)_+ = g_Q^{-2}\left(\tilde{\mathbf{H}} + \tilde{\mathbf{H}}^T\right)\mathbf{y}_Q \cdot 1_{\lambda_Q > 0}(\mathbf{x}_Q, \mathbf{y}_Q), \tag{117}$$

$$\nabla_{\mathbf{x}_Q}\sigma_Q = g_Q^{-2}\left(\tilde{\mathbf{U}} + \tilde{\mathbf{U}}^T\right)\mathbf{x}_Q, \tag{118}$$

$$\nabla_{\mathbf{y}_Q}\sigma_Q = g_Q^{-2}\left(\tilde{\mathbf{U}} + \tilde{\mathbf{U}}^T\right)\mathbf{y}_Q. \tag{119}$$

where $1_{\lambda_Q > 0}(\mathbf{x}_Q, \mathbf{y}_Q)$ is the indicator function, taking the value 1 when $\lambda_Q(\mathbf{x}_Q, \mathbf{y}_Q) > 0$ and 0 otherwise. The definitions of λ_Q and σ_Q are given by equations (74) and (75).

Although we have given an expression for the gradient of $(\lambda_Q)_+$ in eqs. (116) and (117), this choice for the derivative is rather arbitrary; for example an equally valid choice is $\nabla_{\mathbf{x}_Q}(\lambda_Q)_+ = g_Q^{-2}\left(\tilde{\mathbf{H}} + \tilde{\mathbf{H}}^T\right)\mathbf{x}_Q \cdot 1_{\lambda_Q \geq 0}$ since $(\lambda_Q)_+ \equiv \max(0, \lambda_Q)$ is not differentiable at $\lambda_Q = 0$. In fact, these are both special cases of a generalized derivative, and the resulting Jacobians for our Newton method are really *generalized* Jacobians [33] since $\mathbf{f}$ in eq. (58) is only Lipschitz, rather than differentiable due to the $(I_4 - 1)_+^2$ terms. Nevertheless, the Newton method that results can still be superlinearly convergent and there is a large body of work (see for example [34, 35]) that generalizes Newton's method to non-smooth functions.

A.2   Compressible Axisymmetric Model

This model is used to validate the finite element solution in the case where collagen fibers are absent ($\eta = 0$ in all three layers). We consider the radial deformations $r(R)$ of a neo-Hookean, infinitely long and compressible tube. The deformations are uniform with respect to axial distance. We use a strain energy function

$$W = \begin{cases} \dfrac{\mu_1}{2}(I_1 - 3) + \dfrac{\nu\mu_1}{1 - 2\nu}(J_e - 1)^2 - \mu_1 \ln J_e, & A < R < B, \\[2mm] \dfrac{\mu_2}{2}(I_1 - 3) + \dfrac{\nu\mu_2}{1 - 2\nu}(J_e - 1)^2 - \mu_2 \ln J_e, & B < R < C, \\[2mm] \dfrac{\mu_3}{2}(I_1 - 3) + \dfrac{\nu\mu_3}{1 - 2\nu}(J_e - 1)^2 - \mu_3 \ln J_e, & C < R < D, \end{cases} \tag{120}$$

where μ_k, $k = 1, 2, 3$ are the elastic moduli in each of the three layers and ν is the Poisson ratio. The elastic part of the deformation $\mathbf{F}_e = \text{diag}(\alpha_r, \alpha_\theta, 1)$ is diagonal with α_r and α_θ the elastic stretches in the radial and angular directions, so $J_e = \alpha_r\alpha_\theta$ and $I_1 = \alpha_r^2 + \alpha_\theta^2 + 1$. The growth tensor is $\mathbf{G} = \text{diag}(g_0, g_0, 1)$ in the intima and $\mathbf{G} = \mathbf{I}$ in the media and adventitia, so

$$\alpha_r = \begin{cases} r'(R)/g_0, & A < R < B, \\ r'(R), & B < R < D, \end{cases} \tag{121}$$

$$\alpha_\theta = \begin{cases} r/(Rg_0), & A < R < B, \\ r/R, & B < R < D. \end{cases} \tag{122}$$

The radial and tangential stresses are

$$
t_r = \frac{\alpha_r}{J_e} \frac{\partial W}{\partial \alpha_r} = \frac{1}{\alpha_\theta} \frac{\partial W}{\partial \alpha_r}, \tag{123}
$$

$$
t_\theta = \frac{\alpha_\theta}{J_e} \frac{\partial W}{\partial \alpha_\theta} = \frac{1}{\alpha_r} \frac{\partial W}{\partial \alpha_\theta}. \tag{124}
$$

From eqs. (123) and (124), we may write t_r and t_θ as functions of α_r and α_θ, and therefore as functions of $r(R)$ and $r'(R)$:

$$
t_r = G_1(r, r', R) = \begin{cases} \dfrac{\mu_1 r' R}{r} + \dfrac{2\nu\mu_1}{1-2\nu}\left(\dfrac{rr'}{g_0^2 R} - 1\right) - \dfrac{\mu_1 g_0^2 R}{r'r}, & A < R < B, \\[3mm] \dfrac{\mu_2 r' R}{r} + \dfrac{2\nu\mu_2}{1-2\nu}\left(\dfrac{rr'}{R} - 1\right) - \dfrac{\mu_2 R}{r'r}, & B < R < C, \\[3mm] \dfrac{\mu_3 r' R}{r} + \dfrac{2\nu\mu_3}{1-2\nu}\left(\dfrac{rr'}{R} - 1\right) - \dfrac{\mu_3 R}{r'r}, & C < R < D, \end{cases} \tag{125}
$$

$$
t_\theta = G_2(r, r', R) = \begin{cases} \dfrac{\mu_1 r}{r' R} + \dfrac{2\nu\mu_1}{1-2\nu}\left(\dfrac{rr'}{g_0^2 R} - 1\right) - \dfrac{\mu_1 g_0^2 R}{r'r}, & A < R < B, \\[3mm] \dfrac{\mu_2 r}{r' R} + \dfrac{2\nu\mu_2}{1-2\nu}\left(\dfrac{rr'}{R} - 1\right) - \dfrac{\mu_2 R}{r'r}, & B < R < C, \\[3mm] \dfrac{\mu_3 r}{r' R} + \dfrac{2\nu\mu_3}{1-2\nu}\left(\dfrac{rr'}{R} - 1\right) - \dfrac{\mu_3 R}{r'r}, & C < R < D. \end{cases} \tag{126}
$$

The second order ODE for $r(R)$ is:

$$
\frac{dt_r}{dR} + \frac{r'}{r}(t_r - t_\theta) = 0,
$$

$$
\Rightarrow \frac{dG_1(r, r', R)}{dR} + \frac{r'}{r}[G_1(r, r', R) - G_2(r, r', R)] = 0.
$$

Written out in full,

$$
\frac{d}{dR}\left[\frac{Rr'}{r} + \frac{2\nu}{1-2\nu}\left(\frac{r'r}{g_0^2 R} - 1\right) - \frac{g_0^2 R}{r'r}\right] + R\left(\frac{r'}{r}\right)^2 - \frac{1}{R} = 0,
$$

on $A < R < B$, and

$$
\frac{d}{dR}\left[\frac{Rr'}{r} + \frac{2\nu}{1-2\nu}\left(\frac{r'r}{R} - 1\right) - \frac{R}{r'r}\right] + R\left(\frac{r'}{r}\right)^2 - \frac{1}{R} = 0,
$$

on $B < R < C$ and $C < R < D$. Equivalently with $y_1 \equiv r(R)$ and $y_2 \equiv r'(R)$,

$$
\begin{align}
y_1' &= y_2, & A < R < B, & \qquad (127) \\
y_2' F_1(y_1, y_2, R; g_0) + F_2(y_1, y_2, R; g) &= 0, & A < R < B, & \qquad (128)
\end{align}
$$

$$
\begin{align}
y_1' &= y_2, & B < R < C, & \qquad (129) \\
y_2' F_1(y_1, y_2, R; 1) + F_2(y_1, y_2, R; 1) &= 0, & B < R < C, & \qquad (130)
\end{align}
$$

$$
\begin{align}
y_1' &= y_2, & C < R < D, & \qquad (131) \\
y_2' F_1(y_1, y_2, R; 1) + F_2(y_1, y_2, R; 1) &= 0, & C < R < D, & \qquad (132)
\end{align}
$$

where

$$
\begin{align}
F_1(y_1, y_2, R; g_0) &= \frac{R}{y_1} + \frac{1}{g_0^2} \frac{2\nu}{(1 - 2\nu)} \frac{y_1}{R} + \frac{g_0^2 R}{y_2^2 y_1}, \\
F_2(y_1, y_2, R; g_0) &= \frac{y_2}{y_1} + \frac{1}{g_0^2} \frac{2\nu}{(1 - 2\nu)} \frac{y_2^2}{R} - \frac{1}{g_0^2} \frac{2\nu}{(1 - 2\nu)} \frac{y_1 y_2}{R^2} - \frac{g_0^2}{y_1 y_2} + \frac{g_0^2 R}{y_1^2} - \frac{1}{R}.
\end{align}
$$

These coupled equations must be solved with the six boundary conditions

$$
\begin{align}
t_r(A) &= -P, & (133) \\
t_r(B^-) &= t_r(B^+) & (134) \\
t_r(C^-) &= t_r(C^+) & (135) \\
t_r(D) &= 0, & (136) \\
y_1(B^-) &= y_1(B^+), & (137) \\
y_1(C^-) &= y_1(C^+), & (138)
\end{align}
$$

corresponding to an applied lumen pressure at $R = A$, continuity of radial stress at $R = B, C$, no traction at $R = D$, and continuity of deformation at $R = B, C$. This boundary value problem can be solved numerically using Matlab's `bvp4c.m`.